Journal of Non-Newtonian Fluid Mechanics 232 (2016) 102–124

Contents lists available at ScienceDirect

Journal of Non-Newtonian Fluid Mechanics

journal homepage: www.elsevier.com/locate/jnnfm

Viscoplastic flow in an extrusion damper

Alexandros Syrakos[a,*], Yannis Dimakopoulos[a], Georgios C. Georgiou[b], John Tsamopoulos[a]

[a] Laboratory of Fluid Mechanics and Rheology, Department of Chemical Engineering, University of Patras, Patras 26500, Greece
[b] Department of Mathematics and Statistics, University of Cyprus, PO Box 20537, Nicosia 1678, Cyprus

ARTICLE INFO

Article history:
Received 20 January 2016
Accepted 21 February 2016
Available online 13 April 2016

Keywords:
Bingham flow
Viscous damper
Annular cavity
Slip
Viscous dissipation
Finite volume method

ABSTRACT

Numerical simulations of the flow in an extrusion damper are performed using a finite volume method. The damper is assumed to consist of a shaft, with or without a spherical bulge, oscillating axially in a containing cylinder filled with a viscoplastic material of Bingham type. The response of the damper to a forced sinusoidal displacement is studied. In the bulgeless case the configuration is the annular analogue of the well-known lid-driven cavity problem, but with a sinusoidal rather than constant lid velocity. Navier slip is applied to the shaft surface in order to bound the reaction force to finite values. Starting from a base case, several problem parameters are varied in turn in order to study the effects of viscoplasticity, slip, damper geometry and oscillation frequency to the damper response. The results show that, compared to Newtonian flow, viscoplasticity causes the damper force to be less sensitive to the shaft velocity; this is often a desirable damper property. The bulge increases the required force on the damper mainly by generating a pressure difference across itself; the latter is larger the smaller the gap between the bulge and the casing is. At high yield stresses or slip coefficients the amount of energy dissipation that occurs due to sliding friction at the shaft-fluid interface is seen to increase significantly. At low frequencies the flow is in quasi steady state, dominated by viscoplastic forces, while at higher frequencies the fluid kinetic energy storage and release also come into the energy balance, introducing hysteresis effects.

1. Introduction

Viscous dampers dissipate mechanical energy into heat through the action of viscous stresses in a fluid. A common design involves the motion of a piston in a cylinder filled with a fluid, such that large velocity gradients develop in the narrow gap between the piston head and the cylinder, resulting in viscous and pressure forces that resist the piston motion. The potential of such dampers can be enhanced by the use of rheologically complex fluids. For example, use of a shear-thinning fluid such as silicon oil [1,2] weakens the dependency of the damper reaction force on the piston velocity, which is often desirable as it maximises the absorbed energy for a given force capacity. The same effect can be achieved to a higher degree if the fluid is viscoplastic.

Viscoplastic materials flow as liquids when subjected to a stress that exceeds a critical value, but respond as rigid solids otherwise. More specifically, according to the von Mises yield criterion, flow is assumed to occur when the stress magnitude (related to the second invariant of the stress tensor) exceeds a critical value called the yield stress. Such materials are usually concentrated suspensions of solid particles or macromolecules. They are classified as generalised Newtonian fluids because their viscosity depends on the local shear rate, while they do not exhibit elastic effects. Broad surveys of yield-stress materials are given by Bird et al. [3], Barnes [4] and Balmforth et al. [5]. The simplest viscoplastic materials are Bingham fluids, where the magnitude of the stress increases linearly with the rate of strain once the yield stress has been exceeded. Herschel–Bulkley fluids exhibit shear-thinning (or thickening) after yielding.

Damper fluids often exhibit viscoplasticity. For example, electrorheological (ER) and magnetorheological (MR) fluids are suspensions of particles that align themselves in the presence of electric or magnetic fields and form structures that provide the fluid with a yield stress. They can be modelled as Bingham or Herschel-Bulkley fluids whose rheological parameters depend on the strength of the electric or magnetic field [6,7]. Thus, the operation of ER / MR dampers can be tuned by adjusting the field strength. Another example of a damper that works with a yield-stress fluid is the extrusion damper. Here the “fluid” is actually a ductile solid material which is forced to flow through an annular contraction. Such dampers can carry significant loads and

* Corresponding author. Tel.: +302331021265.
E-mail addresses: alexandros.syrakos@gmail.com, syrakos@upatras.gr (A. Syrakos), dimako@chemeng.upatras.gr (Y. Dimakopoulos), georgios@ucy.ac.cy (G.C. Georgiou), tsamo@chemeng.upatras.gr (J. Tsamopoulos).

http://dx.doi.org/10.1016/j.jnnfm.2016.02.011
0377-0257/

have been proposed and used for seismic protection of structures using lead as the plastically-deforming material [8–10]. Lead recrystallises at room temperature and thus recovers most of its mechanical properties immediately after extrusion, so that lead extrusion dampers can undergo a large number of cycles of operation without performance degradation. The present study was motivated by the participation of the authors in a project investigating the design of an extrusion damper employing sand instead of a metallic damping medium. The behaviour of sand is nearly temperature independent, whereas the yield strength of lead drops with the temperature rise that is due to the energy absorption by the damper [11]. Sand is a granular material, and the behaviour of granular materials is known to be described well by the Bingham constitutive equation. Nevertheless, the present study is not limited to this particular design but aims to provide results of greater generality.

In the literature there exist only a few studies on the flow inside viscous dampers, whether viscoplastic or otherwise. Usually, it is assumed that the gap between the piston and the cylinder is narrow enough such that the flow can be approximated by a one-dimensional planar Couette - Poiseuille flow. Although simplified, this analysis can offer some insight on how flow characteristics such as viscoplasticity [12,13], inertia [2,14,15] or viscoelasticity [2,16] affect the damper response. However, it would be desirable to have complete simulations of the flow, which can be assumed to be axisymmetric under normal operating conditions. In the damper literature there appears to be a lack of such studies, with very limited results given in [2,17]. Progress in Computational Fluid Dynamics (CFD) has made such simulations feasible at a relatively modest computational cost.

The goal of the present work is to examine in detail the viscoplastic flow inside a damper whose shaft reciprocates sinusoidally. The fluid is assumed purely viscoplastic of Bingham type; this helps to isolate the effects of viscoplasticity from other phenomena such as shear-thinning, elasticity and thixotropy which may be examined in a future study. The shaft has a protruding spherical bulge that acts like a piston, but in order to investigate the effect of this bulge, the "bulgeless" configuration is also investigated to some extent. The bulged configuration is therefore precisely that of an "extrusion damper" [8–10], whereas the bulgeless configuration is simply the flow in an annular cavity whose inner cylinder reciprocates sinusoidally. The latter is the annular analogue of the popular lid-driven cavity problem, and is of interest on its own. The present simulations span the range of Bingham numbers (Bn) from $Bn = 0$ to $Bn = 320$, which correspond to relatively soft materials (e.g. an ER fluid – see the next Section for the precise details). This allows for the investigation also of inertia effects, which become weaker as the Bingham number is increased. Furthermore, the qualitative behaviour of the damper changes very little beyond some value of the Bingham number, and this behaviour is clearly seen in the present results for $Bn = 320$, so that increasing the Bingham number beyond that would not offer additional insight while at the same time it would significantly increase the computational cost. For simplicity, the effects of temperature increase are not examined and the flow is assumed isothermal, although some results on energy dissipation are included because they pertain to damper operation.

To the best of our knowledge there do not exist any previous studies for the bulged case, but, rather surprisingly, we have not found any studies for the bulgeless case either, with the exception of [18] which, however, focuses on flow instabilities arising at Reynolds numbers significantly higher than those examined here. A related, simpler problem, is the flow in a planar lid-driven cavity with sinusoidal lid motion, for which a few Newtonian studies are available. Among them is that of Iwatsu et al. [19] who performed simulations for a range of Reynolds numbers and oscillation frequencies and found that these parameters have a similar effect on the flow as in Stokes' second problem (sinusoidal oscillation of an infinite plate in an infinite medium); in particular, at low Reynolds numbers and frequencies the flow is in quasi steady state whereas at high Reynolds numbers and frequencies the flow is localised to a thin layer near the lid, while the influence of the lid motion is only weakly felt by the fluid that is farther away. Interestingly, in that paper the force that the lid exerts on the fluid is calculated (a result that is of great interest in the case of dampers); this force is rarely given in lid-driven cavity studies, as the computed value tends to infinity with grid refinement due to the singularities at the lid edges. Therefore, the force reported in [19] is questionable, but nevertheless the results suggest a time lag between the force and the lid velocity which increases with the oscillation frequency. A newer study is [20] which reproduces the findings of Iwatsu et al. [19] and where one can find references to a few other available related published studies.

The oscillating lid-driven cavity problem has not been solved for viscoplastic flow. The closest problem for which we have found results is the even simpler oscillating plate problem (Stokes' second problem), which was solved for viscoplastic flow by Balmforth et al. [21] (this problem has also been solved for other types of non-Newtonian flow - see the literature review in [22]). We should also mention the study of Khaled and Vafai [23] on oscillating plate flow although dealing with Newtonian flow only, because it includes the effects of wall slip; the latter will also be employed in the present study in order to overcome the aforementioned infinite force hurdle. The oscillating plate flow and the present oscillating annular cavity (or damper) flow are driven by the same sinusoidal boundary motion, yet their different geometries lead to significant differences between them. For example, the role of the pressure is trivial in the former and very important in the latter.

On the other hand, if one searches for problems that share a similar geometry to our problem rather than a similar driving force, then the axial viscoplastic Couette–Poiseuille flow through an annulus naturally comes to mind. This problem differs from our own (in the bulgeless case) in that the cylinders extend to infinity rather than form a closed cavity, and the flow is in steady-state; but it could be a good approximation to our flow if the length-to-radius ratio of the cavity is relatively large and the Reynolds number is small enough such that the flow is in quasi steady state. Early solutions of the annular viscoplastic Poiseuille flow (driven by a pressure gradient only) appear in [24,25], while more recent contributions include [26–28], the latter including effects of wall slip. The corresponding solution for annular Couette flow (driven by the axial motion of the inner cylinder only) for a Bingham fluid can be found in [3] (see also Appendix A, where the yield line is given in closed form, something missing from the literature). But the combination of these, i.e. annular Couette–Poiseuille Bingham flow, has only recently been solved for all possible types of flow by Liu and Zhu [29] (another notable contribution is [30]). Daprà and Scarpi [31] move a step closer to our problem by providing results for annular Couette–Poiseuille flow where the pressure gradient and/or the inner cylinder velocity oscillate sinusoidally; however, their focus is on how the flow rate is affected, whereas in order to approximate the flow in a closed annular cavity the instantaneous pressure gradient must be adjusted so that the total flow rate is zero.

The rest of the paper is organised as follows. The problem is defined in Section 2, where the governing equations are also given. Then, in Section 3 an outline of the computational method employed to solve the equations is given, together with references where more details can be found. The results then follow in Section 4, where the effects of viscoplasticity, slip, damper geometry, and oscillation frequency on the damper response are investigated. Finally, conclusions are drawn in Section 5.

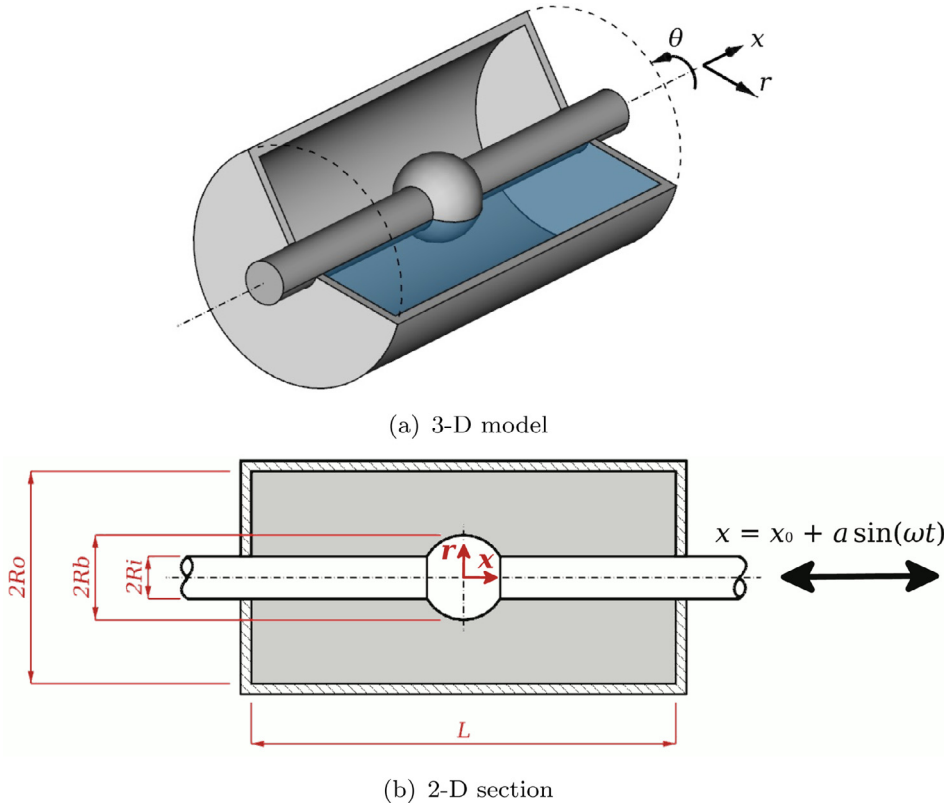

Fig. 1. Layout of the damper. In (a) part of the cylinder is removed to reveal the bulged shaft. The flow is axisymmetric and can be solved on a single plane $\theta = 0$ (coloured in (a)). The viscoplastic material is shown shaded in (b).

2. Problem definition and governing equations

The layout of the damper is shown in Fig. 1. A shaft of radius R_i with a spherical bulge of radius R_b at its centre reciprocates sinusoidally inside a cylinder of bore diameter R_o and length L, filled with a viscoplastic material of Bingham type. A system of cylindrical polar coordinates (x, r, θ) can be fitted to the problem (Fig. 1(a)), with $\underline{e}_x$, $\underline{e}_r$, $\underline{e}_\theta$ denoting the unit vectors along the coordinate directions. The geometry and the flow are assumed to be axisymmetric, so that the solution is independent of θ and the problem is reduced to two dimensions. The fluid velocity is denoted by $\underline{u}$, and its components are denoted by $u = \underline{u} \cdot \underline{e}_x$ and $v = \underline{u} \cdot \underline{e}_r$. The azimuthal velocity component, $\underline{u} \cdot \underline{e}_\theta$, is zero. Initially, the bulge is located midway along the cylinder and the viscoplastic material is at rest. At time $t = 0$ the bulged shaft starts to move, forcing the confined material to flow. The shaft reciprocates along the axial direction such that the $x-$coordinate of any point on the shaft changes in time as

$$x(t) = x_0 + \alpha \sin(\omega t) \tag{1}$$

where x_0 is the position at $t = 0$, α is the amplitude of oscillation, and ω is the angular frequency related to the frequency f by $\omega = 2\pi f$. The period of oscillation is $T = 1/f = 2\pi/\omega$. The velocity of the shaft, dx/dt, is therefore $u_{sh}(t) = U\cos(\omega t)$ where $U = \omega\alpha$ is the maximum shaft velocity. The damper reacts to its imposed motion by a reaction force F_R which dissipates the mechanical energy. The force F_R and the associated energy dissipation are the quantities of interest.

It is assumed that the properties of the material such as the density ρ, the plastic viscosity μ and the yield stress τ_y are constant. The governing equations are the continuity and momentum balances:

$$\frac{\partial \rho}{\partial t} + \nabla \cdot (\rho \underline{u}) = 0 \tag{2}$$

$$\frac{\partial (\rho \underline{u})}{\partial t} + \nabla \cdot (\rho \underline{u}\underline{u}) = -\nabla p + \nabla \cdot \underline{\underline{\tau}} \tag{3}$$

where p is the pressure and $\underline{\underline{\tau}}$ is the deviatoric stress tensor. Due to the density ρ being constant, Eqs. (2) and (3) can be simplified, although these more general forms are shown here. The stress tensor is related to the velocity field through the Bingham constitutive equation,

$$\begin{cases} \underline{\underline{\dot{\gamma}}} = \underline{\underline{0}}, & \tau \le \tau_y \\ \underline{\underline{\tau}} = \left(\dfrac{\tau_y}{\dot{\gamma}} + \mu\right)\underline{\underline{\dot{\gamma}}}, & \tau > \tau_y \end{cases} \tag{4}$$

where $\underline{\underline{\dot{\gamma}}}$ is the rate-of-strain tensor, defined as $\underline{\underline{\dot{\gamma}}} \equiv \nabla \underline{u} + (\nabla \underline{u})^{\mathrm{T}}$. The tensor magnitudes, $\tau \equiv (\frac{1}{2}\underline{\underline{\tau}} : \underline{\underline{\tau}})^{1/2}$ and $\dot{\gamma} \equiv (\frac{1}{2}\underline{\underline{\dot{\gamma}}} : \underline{\underline{\dot{\gamma}}})^{1/2}$, also appear in the above equation. Thus, the material flows only where the magnitude of the stress tensor exceeds the yield stress.

An aspect of the problem that complicates things is the fact that at the contact points between the shaft and the flat sides of the cylinder the velocity jumps discontinuously from non-zero values at the moving shaft to zero at the cylinder. If the no-slip boundary condition is used, this results in stress varying as $1/\delta x$ where δx is the distance from the discontinuity [32], and the force exerted on the shaft becomes infinite. This result is spurious, and in fact molecular dynamics simulations have shown that the no-slip boundary condition is to be blamed, being unrealistic near the singularities where an amount of slip is exhibited that bounds the stress and the total force to finite values [33,34]. In fact, even without the corner singularity, when it comes to viscoplastic flows, wall

slip appears to be the rule rather than the exception [35]. Navier slip is the simplest alternative to the no-slip boundary condition, but nevertheless it is asserted in [34] that it is a realistic condition for Newtonian flows with corner singularities. It bounds the stress distribution and makes it integrable so that the total force can be calculated, as shown in [36].

According to the Navier slip condition, the relative velocity between the fluid and the wall, in the tangential direction, is proportional to the tangential stress. More formally, for two-dimensional or axisymmetric flows such as the present one, this is expressed as follows: Let $\underline{n}$ be the unit vector normal to the wall, and $\underline{s}$ be the unit vector tangential to the wall within the plane in which the equations are solved. Let also $\underline{u}$ and $\underline{u}_w$ be the fluid and wall velocities, respectively. Then,

$$(\underline{u}-\underline{u}_w)\cdot\underline{s}=\beta(\underline{n}\cdot\underline{\underline{\tau}})\cdot\underline{s} \tag{5}$$

where the parameter β is called the slip coefficient.

For non-Newtonian flows the slip behaviour may be more complex than that described by the Navier slip condition; for example, the slip velocity and the wall stress may be related by a power-law relationship [37], or there may be a "slip yield stress", that is, slip may occur only if the wall stress has exceeded a certain value [38]. A recent review of wall slip possibilities in non-Newtonian flows can be found in [39]. Concerning the present application, the interface between the shaft and the extruded material is often lubricated and the shaft surface is polished [8,9]. Hence, in the present study, in order not to overly increase the complexity of the problem, it was decided to apply the simple Navier slip boundary condition on the polished shaft and the no-slip boundary condition (Eq. (5) with $\beta=0$) on the cylinder bore, whose surface has no special treatment.

It will be useful to express the governing equations in dimensionless form. So, let lengths be normalised by the distance between the shaft and the cylinder $H=R_o-R_i$, velocities by the maximum shaft speed U, time by the oscillation period T, and pressure and stresses by a characteristic stress $\tau_{\text{ref}}=\tau_y+\mu U/H$. The latter is composed of a plastic component (τ_y) and a viscous component ($\mu U/L$) in order to better represent a typical viscoplastic stress. Then, combining Eq. (3) with Eq. (4), and using the fact that ρ is constant, one obtains for the yielded part of the material

$$Re^*\left(\frac{1}{Sr}\frac{\partial\tilde{\underline{u}}}{\partial\tilde{t}}+\tilde{\nabla}\cdot(\tilde{\underline{u}}\tilde{\underline{u}})\right)=-\tilde{\nabla}\tilde{p}+\frac{Bn}{Bn+1}\tilde{\nabla}\cdot\left[\left(\frac{1}{\tilde{\dot{\gamma}}}+\frac{1}{Bn}\right)\tilde{\underline{\underline{\dot{\gamma}}}}\right] \tag{6}$$

where tildes ($\tilde{}$) denote dimensionless variables. Note that the dimensionless rate-of-strain tensor and its magnitude are equal to their dimensional counterparts normalised by U/H. Eq. (6) contains three dimensionless numbers. The Bingham number Bn, defined as

$$Bn\equiv\frac{\tau_y}{\mu U/H} \tag{7}$$

is a measure of the viscoplasticity of the flow. The effective Reynolds number Re^* [40] is defined as

$$Re^*\equiv\frac{\rho U^2}{\tau_y+\mu\frac{U}{H}}=\frac{\rho U^2}{\tau_{\text{ref}}}=\frac{Re}{Bn+1} \tag{8}$$

and is an indicator of the ratio of inertia forces to viscoplastic forces, just like the usual Reynolds number $Re\equiv\rho U^2/(\mu U/H)=\rho UH/\mu$ is an indicator of the ratio of inertia forces to viscous forces. Finally, the Strouhal number Sr is defined as

$$Sr\equiv\frac{T}{H/U} \tag{9}$$

From $T=2\pi/\omega$ and $U=\omega\alpha$ it follows that $Sr=2\pi\alpha/H=2\pi A$, where $A=\alpha/H$ is the dimensionless amplitude of oscillation.

Table 1
Values of the dimensional and dimensionless parameters defining the base case.

Fluid properties	$\rho=1000\text{kg/m}^3$, $\mu=1.0\text{Pa s}$, $\tau_y=31.416\text{Pa}$
Geometry	$R_i=10$ mm, $R_o=50$ mm, $R_b=20$ mm, $L=200$ mm
Oscillation	$f=0.5$ Hz, $\alpha=20$ mm
Slip	$\beta=4.7619\times10^{-5}$ m/Pa s ($l=4.7619\times10^{-5}$ m)
Dimensionless parameters	$Re^*=0.12$ ($Re=2.51$), $Sr=3.14$, $Bn=20$, $\tilde{\beta}=0.025$ ($\tilde{l}=1.19\times10^{-3}$), $R_i/R_o=0.2$, $R_b/R_o=0.4$, $L/H=5$

Therefore, the fact that the characteristic velocity U is inherently inversely proportional to the characteristic time T removes the dependance of Sr on T. So, Sr is only a dimensionless expression of the amplitude.

The boundary conditions are also expressed in nondimensional form. On the motionless cylinder walls where the no-slip condition applies, the boundary condition is just $\tilde{\underline{u}}=0$. The dimensionless shaft velocity is $\tilde{u}_{sh}=\cos(2\pi\tilde{t})$, and can be seen not to depend on any of the dimensionless numbers. However, another dimensionless number enters through the dimensionalisation of the Navier slip condition (5), which is applied on the shaft:

$$(\tilde{\underline{u}}-\tilde{\underline{u}}_{sh})\cdot\underline{s}=\tilde{\beta}\left(\underline{n}\cdot\tilde{\underline{\underline{\tau}}}\right)\cdot\underline{s} \tag{10}$$

The dimensionless Navier slip coefficient is given by:

$$\tilde{\beta}\equiv\frac{\beta\mu}{H}(Bn+1)=\tilde{l}(Bn+1) \tag{11}$$

where $l=\beta\mu$ is the slip (or extrapolation) length and $\tilde{l}=l/H$ is its dimensionless counterpart. In Newtonian flows the use of the slip length is preferred to the use of the slip coefficient, and therefore in the simulations we will occasionally mention the values of the slip length as well.

Finally, three additional dimensionless numbers are needed to determine the boundary geometry. Different choices are possible. One such choice leads to the following set of seven dimensionless variables that define the problem: Re^*, Sr, Bn, $\tilde{\beta}$, R_i/R_o, R_b/R_o and L/H.

The code used for the simulations solves the dimensional equations. However, the results will be presented mostly in dimensionless form because this form offers greater insight into the phenomena and greater generality. An important result for the present application is the force acting on the shaft, which in the present study is dedimensionalised by a reference force F_{ref}:

$$F_{\text{ref}}=(2\pi R_iL)\tau_{\text{ref}}\quad\text{where}\quad\tau_{\text{ref}}=\tau_y+\mu U/H \tag{12}$$

Thus the reference force is that which results from the reference stress τ_{ref} acting on the whole shaft surface, of area $2\pi R_iL$, in the absence of a bulge.

Due to the large number of parameters, it was decided to set a base case, which is defined in Table 1, and then vary several of the problem parameters, each in turn, in order to investigate their effect on the damper response. The base case was defined using typical values for the parameters, choosing values that lie in the parameter range of the damper literature cited in Section 1 and result in "nice" (rounded) values of the dimensionless parameters. In particular: The geometry is of the "extrusion" type and is closer to the compact design of [10] rather than the older, bulky designs of [8,9]. The oscillation amplitude is near the average of that found in the referenced studies (e.g. [1,13,15,41]), while the base frequency is near the low end of the spectrum of frequencies in the referenced studies. For example, for seismic applications frequencies in the range 0.1 – 2.5 Hz are reported in [41], but they can be as high as 10 Hz for short buildings [16]. Here the chosen base frequency is 0.5 Hz but numerical experiments with frequencies of up to 8 Hz are performed in Section 4. The rheological properties resemble

those of an ER or MR fluid, modelled as a Bingham fluid, [12,16,17], with yield stresses of up to 500 Pa employed in Section 4.

Finally, we note that the present results do not apply to lead extrusion dampers since metal extrusion is governed by other constitutive equations, where plasticity is dominant. However, such equations are not much different than viscoplastic constitutive equations such as the Bingham equation in the limit of high plasticity; for example, in [42] metal extrusion is modelled using a regularised Levy–Mises flow rule to which the Bingham equation reduces when $\mu = 0$. In fact, the methodology and finite volume solution method of that study are very similar to those employed in the present study. The Bingham constitutive equation, which is adopted here, allows the investigation of inertial, viscous, and plastic effects and therefore gives more generality to the results. As will be seen in Section 4, in the present numerical experiments, at the higher Bingham numbers tested here plasticity is also dominant over other flow mechanisms (inertia, viscosity). Another study where the finite volume methodology is applied to solve metal extrusion problems is [43], where further references can be found.

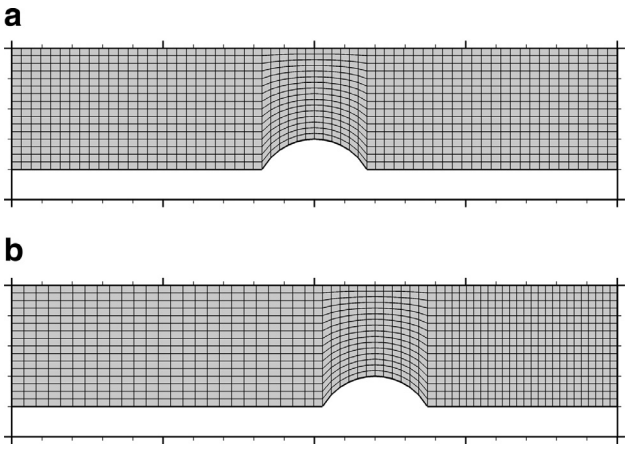

Fig. 2. Sample grids, (a) at a time instant when the bulge is located midway along the cylinder, and (b) at a time when the bulge is offset towards the right. For clarity, coarse 64 × 16 volume grids are shown instead of the 1024 × 256 grids actually used.

3. Numerical method

The problem defined in Section 2 was solved using a finite volume method, which will be described in the present section only briefly, providing pertinent references. A detailed description of the method will be presented in a separate publication. It is an extension of that presented in [44,45], with extensions for transiency, axisymmetry, grid motion and the slip boundary condition.

The method employs second-order accurate central differences for both the convective and viscous terms, with correction terms included to account for grid non-orthogonality, skewness and stretching [44]. All variables are stored at the volume centres and spurious pressure oscillations are avoided by the use of momentum interpolation [44,46]. The gradients of the flow variables are calculated using a least-squares procedure [47]. These gradients are needed for the calculation of the aforementioned correction terms and also for the calculation of the magnitude of the rate-of-strain tensor and hence of the viscosity (Eq. (13) below). Time derivatives are approximated by a fully implicit, second-order accurate three-time-level backward differencing scheme [48]. To account for axisymmetry, the original planar finite volume code was adjusted as described in [48], and, in addition, the calculation of the magnitude of the rate-of-strain tensor must take into account that the component $\dot{\gamma}_{\theta\theta} = 2v/r$ is, in general, non-zero.

Since it is axisymmetric, the problem can be solved in any single $x - r$ plane. Such a plane is partitioned into a number of finite volumes, using grids of sizes of 1024 × 256 volumes in the x- and r-directions, respectively. When the shaft is bulgeless, the grid is stationary; but when a bulged shaft is used the grid changes in time to follow the deformation of the domain due to the bulge motion. Fig. 2 shows a couple of coarser grids at different time instances. The grid above the bulge and small margins on either side of it along the x-direction remains fixed, while the rest of the grid is compressed / expanded accordingly as the bulge moves.

Grid motion requires that the convective terms of the equations use the relative velocity of the fluid relative to the volume faces, rather than the absolute fluid velocity. In the present method this is implemented by a scheme that ensures that the so-called *space conservation law* [49] is obeyed, i.e. that the fluid volume "swallowed" by the faces during a time step is equal to the volume increase of the cell that owns the faces. The details will be presented in a future publication, but we note that in the present case such a specialised scheme is not really necessary as the fact that only one set of grid lines move ensures space conservation anyway [49].

A difficulty with simulations involving yield stress fluids is that the domain of application of each branch of their constitutive equation, such as (4), is not known in advance. A popular approach to overcoming this difficulty is to approximate Eq. (4) by a regularised equation which is applicable throughout the material without branches. Several such regularised equations have been proposed; some of them are compared in [50]. In the present work we adopt the one proposed by Papanastasiou [51], which is perhaps the most popular and has been used successfully for simulating many flows of practical interest (see, e.g., [52–55], among many others). It is formulated as follows:

$$\underline{\underline{\tau}} = \left[\frac{\tau_y}{\dot{\gamma}}\left(1 - \mathrm{e}^{-m\dot{\gamma}}\right) + \mu\right]\underline{\underline{\dot{\gamma}}} = \eta(\dot{\gamma})\underline{\underline{\dot{\gamma}}} \tag{13}$$

or, in non-dimensional form:

$$\underline{\underline{\tilde{\tau}}} = \frac{Bn}{Bn+1}\left[\frac{1 - e^{-M\tilde{\dot{\gamma}}}}{\tilde{\dot{\gamma}}} + \frac{1}{Bn}\right]\underline{\underline{\tilde{\dot{\gamma}}}} = \tilde{\eta}(\dot{\gamma})\underline{\underline{\tilde{\dot{\gamma}}}} \tag{14}$$

where the term in square brackets in Eq. (13), η, is the effective viscosity and m is a stress growth parameter which controls the quality of the approximation: the larger this parameter the better Eq. (13) approximates (4). This parameter is nondimensionalised as $M = mU/H$. Increasing the value of M also makes the equations stiffer and harder to solve, so a compromise must be made. In our previous study for the lid-driven cavity test case [45] it was found that increasing M beyond 400 caused numerical problems. However, in the present case it was possible to use a value of $M =$ 1000. Thus, Eq. (13) assumes all of the material to be a generalised Newtonian fluid whose effective viscosity is given by the term in square brackets, and the unyielded material is approximated by assigning very high values to the viscosity. To identify the unyielded material we employ the usual criterion $\tau < \tau_y$, or, in terms of dimensionless stress, $\tilde{\tau} < \tilde{\tau}_y = \tau_y/\tau_{\mathrm{ref}} = Bn/(Bn+1)$ (the ratio $Bn/(Bn+1)$ is sometimes called the *effective Bingham number* Bn^* [40]); see [56,57] for discussions on the use of this criterion.

The use of a regularised constitutive equation is also justified by the fact that experiments have not shown definitively that the transition from solid-like to fluid behaviour is completely sharp [4]. In this respect, Eq. (13) could be regarded as a more realistic constitutive equation. Nevertheless here it will be considered an approximation to Eq. (4). The accuracy of the regularisation approach to solving viscoplastic flows is discussed in [50,58]; their main disadvantage is the difficulty sometimes exhibited in accurately capturing the yield surfaces, but for the present application this is not of main concern. For alternative approaches, see [58,59].

To ensure that the value $M = 1000$ is sufficient to obtain an accurate solution, a series of steady-state simulations was performed with varying values of M, where a shaft without a bulge moves at a constant velocity equal to the maximum velocity of the base case (Table 1; $U = 2\pi f\alpha$). The dimensionless numbers for this steady-state problem have the same values as in Table 1, except for the Strouhal number which is infinite, due to the problem being steady-state. So, solving this steady state problem we obtain values of 2.01988, 2.02156, 2.02241 and 2.02286 for the nondimensional force $\tilde{F}$ exerted on the shaft, for M = 125, 250, 500 and 1000, respectively. The dependency of the force on M appears to be weak, with the force values $F(M)$ converging towards a value, say F^*. If it is assumed that convergence of $F(M)$ to F^* follows the formula $F(M) = F^* + cM^{-q}$, where q is the order of convergence and c a constant, then q can be estimated using the results from using three different values of M related through a fixed ratio, say M, $2M$ and $4M$, to give:

$$q = \frac{\log\left(\frac{F(M)-F(2M)}{F(2M)-F(4M)}\right)}{\log(2)} \tag{15}$$

Applying this formula to the above values gives $q \approx 1$, which means that doubling the value of M reduces the error cM^{-q} to half. This result can be used to estimate the error $F^* - F(M) \approx [F(M) - F(M/2)]/(2^q - 1) = F(M) - F(M/2)$ (for $q = 1$). Therefore, the error due to regularisation at $M = 1000$ is about 0.02%, which is very small. In fact, for most engineering applications, even lower values of M would provide acceptable accuracy.

The system of non-linear algebraic equations that arises from the discretisation is solved using the SIMPLE algorithm [60] with multigrid acceleration. The Navier slip condition can be easily accounted for in SIMPLE using the deferred correction approach of Khosla and Rubin [61]. The details will be provided in a forthcoming publication focusing on the numerical method employed here. Alternative treatments, including treatments for more complicated slip conditions, can be found in [62].

An important issue concerning numerical solutions is grid convergence: the grid must be fine enough so that the solution is sufficiently accurate. The existence of singularities at the grid corners does not pose problems concerning the bulk of the flow; thus, the accuracy of the present method for grids of resolution comparable to the present case is demonstrated in [45,57]. But the present study examines a new result, the force exerted on the shaft, and it turns out that the accuracy of this result is heavily affected by the singularities at the shaft endpoints. The reason is the following. As discussed in Section 2, the Navier slip boundary condition results in finite stress and pressure at the shaft endpoints for any $\beta \neq 0$. However, the smaller the value of β the larger the stress and pressure there, and the larger the overall force on the shaft, tending to infinity as $\beta \to 0$. So, by varying the slip parameter the shaft force can obtain values in the whole range from zero to infinity. Using smaller values of β results in steeper rise of the stress near the shaft ends, which requires finer grids to maintain an accurate calculation of the force. The present section therefore ends with a grid convergence study.

Fig. 3 (a) demonstrates that grid convergence of the stress distribution near the corners is much faster when $\tilde{\beta}$ is large than when it is small. Column "$Bn = 20$" of Table 2 lists the computed values of force on grids of varying density for a steady-state variant of the base case of Table 1 without a bulge, along with the order of grid convergence. Up to the 512 × 128 grid the force decreases with grid refinement and appears to converge with order $q = 2$, but on the 1024 × 256 grid the force increases slightly. This behaviour can be explained, with reference to Fig. 3(a), by the fact that grid refinement causes the computed stress to decrease over most of the length of the shaft, except near the ends where it increases due to the singularities. At high grid densities the stress increase near the corners dominates over the stress decrease over the rest of the shaft because the latter has already converged, whereas the former has not. The need therefore arises to estimate the force error on the 1204 × 256 grid, and assess whether it is acceptable.

Table 2
Computed values of (dimensional) force on the shaft as a function of the grid density, for a couple of steady state problems. The problem parameters are listed in Table 1, with a constant shaft velocity of $U = 2\pi f\alpha$, and there is no bulge. In addition, the second problem involves Newtonian flow ($\tau_y = Bn = 0$). The grid convergence index q is calculated from formula (15) if M is replaced by the number of volumes in either the x- or the r-direction.

Grid size	$Bn = 20$	q	$Bn = 0$	q
128 × 32	0.8643		0.1372	
256 × 64	0.8436		0.1475	
512 × 128	0.8379	1.85	0.1565	0.21
1024 × 256	0.8385	–	0.1635	0.34
2048 × 512			0.1683	0.56
4096 × 1024			0.1710	0.84
8192 × 2048			0.1722	1.12

The error can be estimated by comparing against the solution on a finer grid, but due to the deterioration of the SIMPLE/multigrid algorithm on Bingham problems which is discussed in [45] this is not practical. A more appropriate treatment would be to use adaptively refined grids with large densities near the corners, using techniques such as those described in [57]. However, the adaptive mesh refinement algorithm has not yet been extended to time-dependent problems and moving grids in the available code. So, it was decided instead to solve a Newtonian steady-state problem (which is easier to solve) on a series of very fine grids with up to 8192 × 2048 volumes, and estimate the error of that problem. The results are also listed in Table 2, and they show that the force value does converge, although the full second-order rate of convergence has not yet been attained even on the finest grid. Assuming that the rate of convergence on grid 8192 × 2048 is approximately first order, the error on grid 1204 × 256 is estimated at about 0.01 N, or 0.01 / 0.17 = 6% which is rather large. But for higher Bingham numbers this percentage drops, as Fig. 4 suggests. The large stresses near the shaft ends are due to steep velocity gradients, which induce stress components related to fluid deformation, $\mu\underline{\underline{\dot{\gamma}}}$. When the yield stress τ_y is increased, the proportion of the deformation-induced component $\mu\underline{\underline{\dot{\gamma}}}$ within the total stress $\tau_y(\underline{\underline{\dot{\gamma}}}/\dot{\gamma}) + \mu\underline{\underline{\dot{\gamma}}}$ falls. So, assuming that the component $\mu\underline{\underline{\dot{\gamma}}}$ does not change much between the $Bn = 0$ and $Bn = 20$ cases, the force error on grid 1024 × 256 for the $Bn = 20$ case of Table 2 would also be about 0.01 N, or 0.01 / 0.84 = 1.2%, which is acceptable. So, the value $\tilde{\beta} = 0.025$ selected for the base case offers accurate computation of the shaft force on the 1024 × 256 grid, while at the same time Fig. 3(b) suggests that it results in a flow field that is negligibly different from that of the no-slip condition, except very close to the ends of the shaft.

For the temporal discretisation a time step of $\Delta t = T/400$ was used; it will be shown in Section 4 that the time step size has a small effect on the accuracy, because for most of the test cases studied the temporal term in the momentum equation is small compared to the other terms.

4. Results

We start with a general description of the flow inside the damper for the base case, which is visualised in Fig. 5. A first observation is that at the extreme points of the shaft motion, Fig. 5(a) and (b), when the shaft velocity is zero, the fluid velocity is also

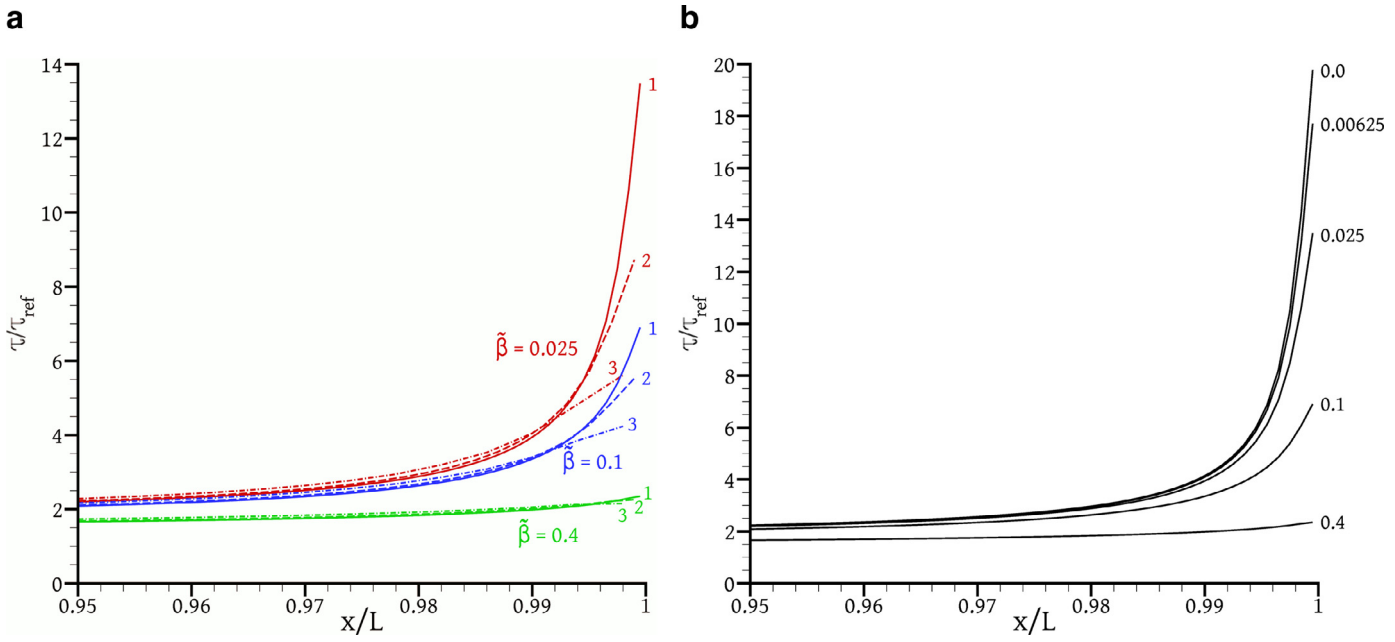

Fig. 3. Nondimensional shear stress distributions $\tilde{\tau}_{rx}$ along the shaft surface near the end of the shaft, for a steady state problem (shaft velocity $= U = 2\pi f\alpha$) without a bulge. The problem parameters are as displayed in Table 1, except for the slip coefficient, which is varied to obtain the non-dimensional values indicated on each figure. In (a) the stress is plotted for $\tilde{\beta} = 0.025$ (red), 0.1 (blue) and 0.4 (green), as calculated on grids 1 (1024 × 256 volumes), 2 (512 × 128 volumes) and 3 (256 × 64 volumes). In (b) the stress is plotted for different values of $\tilde{\beta}$, indicated on each curve, calculated on a 1024 × 256 grid. (For interpretation of the references to colour in this figure legend, the reader is referred to the web version of this article).

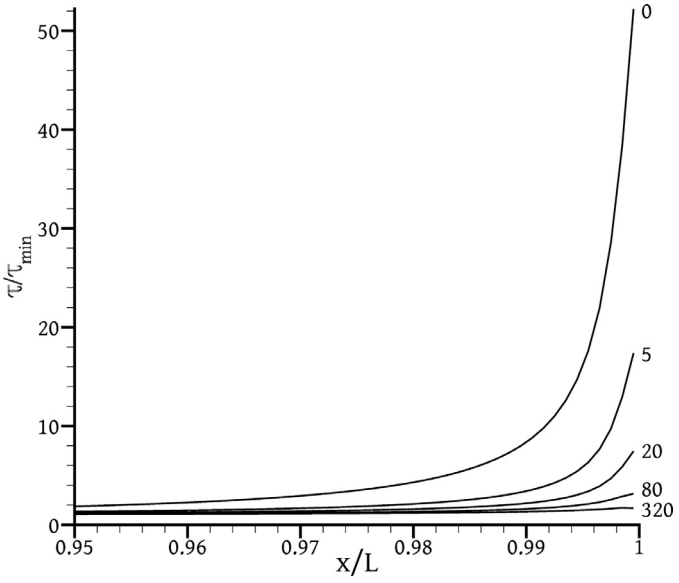

Fig. 4. Shear stress $\tilde{\tau}_{rx}$ along the shaft surface near the end of the shaft, for a steady state problem without a bulge, for various Bingham numbers, as computed on the 1024 × 256 grid. For each *Bn*, the stress is normalised by its minimum value along the shaft. The problem parameters are as displayed in Table 1, except that the shaft velocity is constant at $U = 2\pi f\alpha$, there is no bulge, and the value of the yield stress is chosen so as to obtain the Bingham numbers shown.

zero and the material is in fact completely unyielded. The same observation has been made for almost all test cases studied in the present work, except for Newtonian flow and flow at high frequency. Therefore, there is no point in extending the duration of each simulation beyond a single period T, as the flow has already reached a periodic state from $t = T/4$. For a few exceptional cases we extended the simulation duration to two periods, although the results which will be presented in this paragraph show that the periodic state is reached sooner.

As the shaft retracts from its extreme right position and accelerates (left column of snapshots in Fig. 5), increasingly more of the material yields. The amount of yielded material becomes maximum when the shaft is at its central position and its velocity is maximum (Fig. 5(i)); at this point the unyielded material is restricted only to the outer corners of the cylinder. Yet, most of the flow occurs in the vicinity of the bulge, as shown by the density of the streamlines. The bulge motion causes the fluid immediately downstream of it to be pushed out of the way, and following a circular-like path it is transported behind the bulge. Away from the bulge, the fluid, although mostly yielded, moves extremely slowly.

The right column of snapshots in Fig. 5 corresponds to time instances when the shaft displacement and velocity are either equal or opposite to that of the snapshot immediately to the left. It is evident from comparing the left and right columns of the figures that symmetry or equality in the instantaneous boundary conditions implies also symmetry or equality of the flow field. The flow history does not play a significant role; it is mostly the instantaneous boundary conditions that determine the flow field. This can be attributed to the low Reynolds number of the base case, $Re^* = 0.12$ (Table 1) which makes the left hand-side of the momentum Eq. (6), i.e. the inertia forces, very small compared to the right hand side (pressure and viscoplastic forces). The time derivative term in the left-hand side of Eq. (6) thus plays an insignificant role and the flow is in a quasi steady state where at each time instance the flow field is determined by the instantaneous boundary conditions and not by the history of the flow. As a side-effect, the accuracy of the simulation depends only weakly on the time step Δt.

A feel of the effect of the bulge can be obtained by comparing the snapshots of Fig. 6, obtained also for the parameters of the base case but in the absence of a bulge, against those in the left column of Fig. 5. The bulge causes larger stresses in its vicinity, causing more of the material to yield. The streamline pattern shows that it also causes significant flow around it as it moves. On the contrary, in the absence of a bulge the streamline pattern shows that the motion of the material is concentrated in a

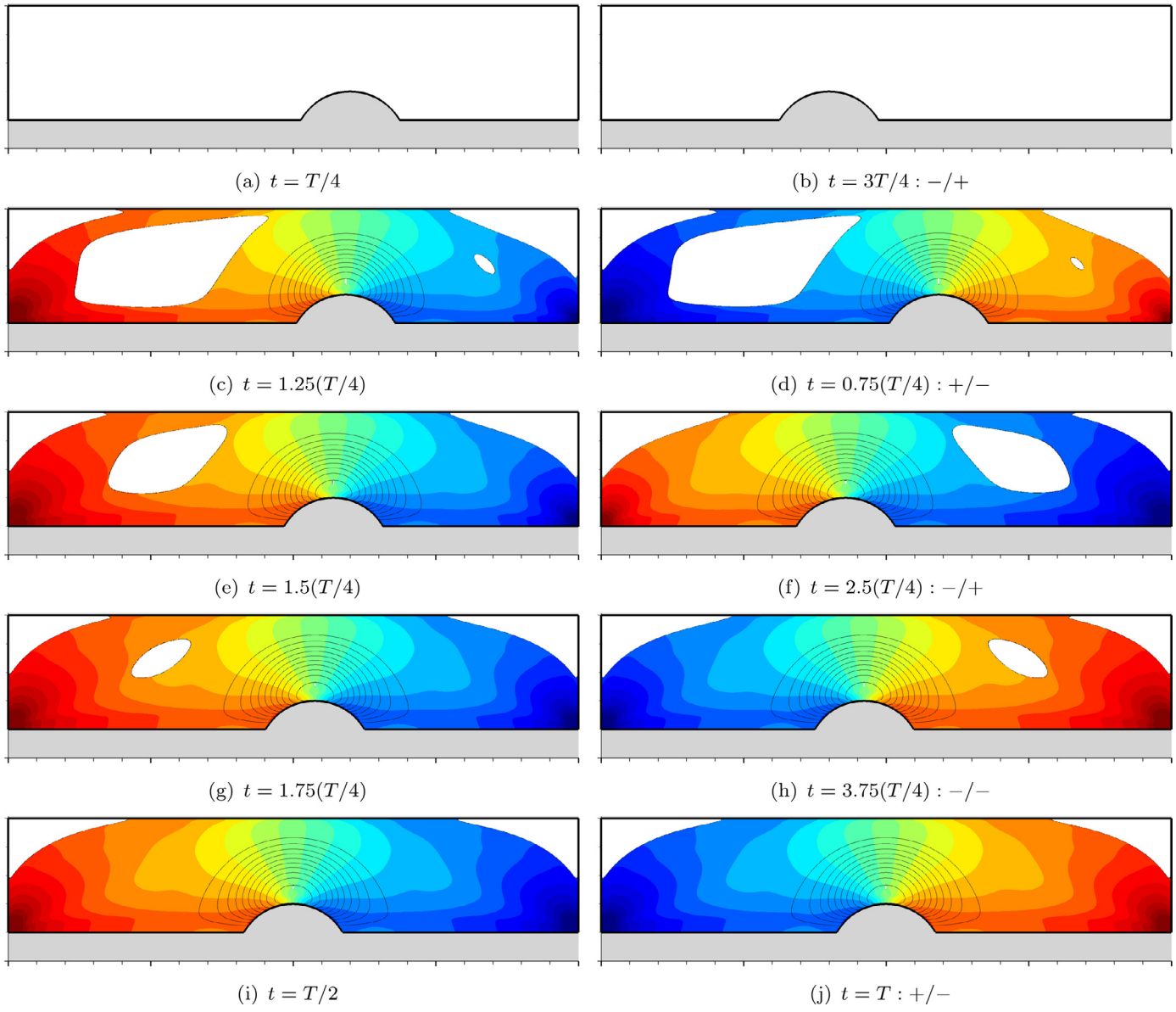

Fig. 5. Snapshots of the flow field for the base case (Table 1). The shaft is shown in grey. The black lines are streamlines; within each figure they correspond to equispaced values of the streamfunction, from zero (at motionless walls) to the instantaneous maximum value. The colour contours represent dimensionless pressure $\tilde{p} = p/\tau_{\text{ref}}$, in the range from -10 (blue) to $+10$ (red) with a step of 0.8. Regions of unyielded material ($\tau < \tau_y$) are shown in white. The left column of figures are in chronological order from top to bottom, starting with the shaft motionless in its extreme right position at time $t = T/4$ (a) and ending with the shaft in the middle position, moving with maximum velocity, at time $t = T/2$ (i). The right column of figures is not in chronological order, but each figure exhibits some sort of symmetry compared to the figure immediately to its left. This is indicated with a pair of signs in the caption of each figure in the form D/U, where D is a "+" if the displacement of the shaft is the same as in the figure immediately on the left, and a "−" if it is opposite to that, and U gives the same information for the shaft velocity. (For interpretation of the references to colour in this figure legend, the reader is referred to the web version of this article).

very thin layer close to the shaft, whereas in the rest of the domain the material moves very slowly. Also, the variation of the size and shape of the unyielded regions during the oscillation is weaker than in the bulged shaft case; in fact in the bulgeless case, throughout the oscillation, the central unyielded plug zone extends over most of the domain leaving only thin yielded layers over the shaft and outer cylinder, while its axial extent varies weakly with time.

In the paragraphs that follow, the effect of various parameters on the flow is examined.

4.1. Effect of viscoplasticity

The most important result of the simulations is the damper reaction force F_R as a function of the shaft displacement or velocity. This force can be analysed into two components, a viscoplastic component $\int_{sh} \underline{n}\cdot\underline{\underline{\tau}}\, dA$ and a pressure component $\int_{sh} -p\underline{n}\, dA$, where integration is over all the shaft surface and $\underline{n}$ is the unit vector normal to this surface. Due to symmetry, the net force is in the axial direction $\underline{e}_x$ only. Fig. 7 shows how the total force and its separate viscoplastic and pressure components are affected by the viscoplasticity of the material. The different curves correspond to materials with different yield stress, while the rest of the material properties are the same, as listed in Table 1. The Bingham number, being representative of the viscoplasticity of the material, is used to differentiate between the curves, but by changing the yield stress other dimensionless numbers change as well: the effective Reynolds number Re^* (but not the usual Re) decreases as τ_y increases (Eq. (8)), reflecting the fact that by increasing the yield stress the viscoplastic forces become more dominant over inertia;

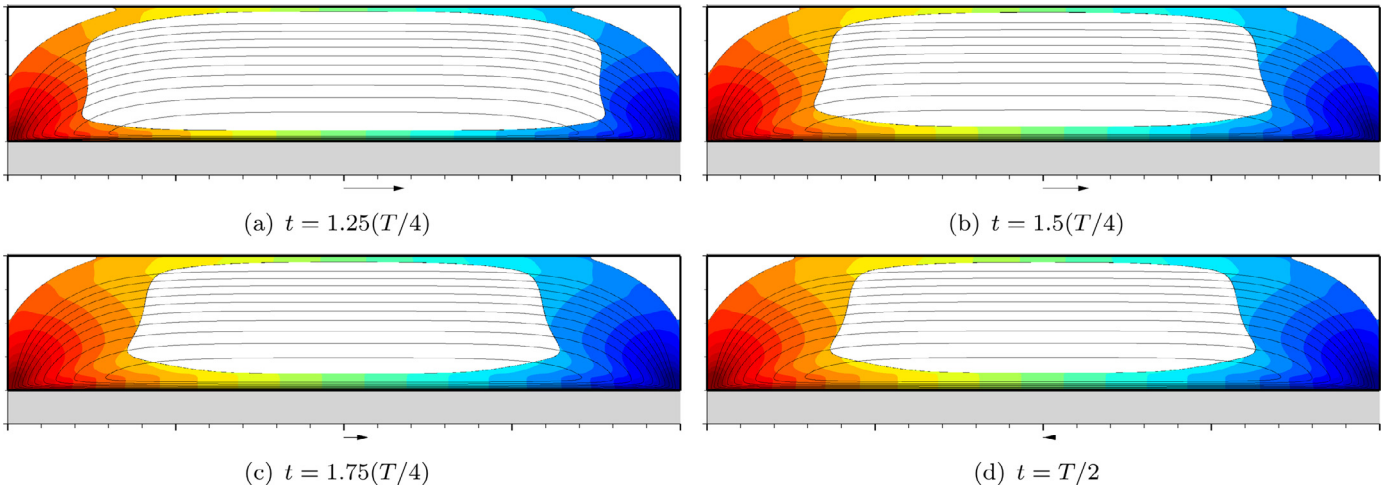

Fig. 6. Snapshots of the flow field for the base case (Table 1) in the absence of a bulge. See caption of Fig. 5 for details. The arrow below each figure indicates the shaft displacement. The snapshots correspond to the times of the left column of figures in Fig. 5. At $t = T/4$ the material is completely unyielded.

and the slip coefficient $\tilde{\beta}$ (Eq. (11)) increases as τ_y increases, reflecting the fact that, for a given shaft velocity U, increasing τ_y generally increases the overall levels of stress in the domain leading to more slip at the walls.

The effect of viscoplasticity is summarised in Fig. 7(a). At time $t = 0$ the material is initially at rest, but the shaft suddenly starts to move towards the right at a finite velocity of $U = \alpha\omega$. This creates a very large initial inertial reaction force (towards the left, i.e. with negative sign) whose magnitude drops very rapidly due to the small value of Re^*; this drop is illustrated by the nearly vertical part of the curves at zero displacement. The test case where the relative importance of inertia is greatest is the Newtonian case ($Bn = 0$) where indeed the initial force drop can be seen to be more gradual, but nevertheless the periodic state is quickly attained when the displacement is about 0.4α and from that point on the force at time t is indistinguishable from that at time $t + T$ (the Newtonian case was solved for a duration of $2T$). The force–displacement curves for $Bn = 0$, and to a lesser extent for $Bn = 5$, are skewed; that is, the reaction force is smaller when the shaft is approaching an extreme position $x = \pm\alpha$ and decelerating, than when it is retracting from it and accelerating. This is due to inertia: when the shaft is accelerating then it also has to accelerate the surrounding fluid, whereas when it is decelerating it does not have to do so because the fluid has already acquired momentum in the direction of motion. This effect is insignificant when the viscous forces greatly surpass the inertia forces, i.e. at low Re^* numbers. This is shown more clearly in the force–velocity diagram, Fig. 7(d), where the curves for $Bn = 0$ and 5 exhibit some hysteresis, i.e. the force does not depend only on the current velocity but also on the flow history. For each shaft velocity there are two values of force: a higher one, when the shaft is accelerating, and a lower one, when it is decelerating. On the contrary, for $Bn \geq 20$ no such hysteresis is observable, and the curves are symmetric with respect to the zero displacement line in Fig. 7(a). Thus for these cases Re^* is so small that the inertia terms in Eq. (6) are negligible. The weakening of the hysteresis effect with increasing the Bingham number can be seen in the experimental results reported in [14].

In the diagrams of Fig. 7 the force is dimensionalised by F_{ref}, Eq. (12), and so increasing τ_y makes the force appear smaller whereas in fact it becomes larger. The obvious effect of increasing τ_y is to make the force curves flatter, i.e. the larger τ_y the less the force varies during the motion of the shaft. For some applications this is considered an advantage of the damper, since it maximises the energy absorbed for a given force capacity. The explanation is simple: the total viscoplastic stresses consist of two components, one of constant magnitude (plastic) and one of variable magnitude (viscous), $\tau = \tau_y + \mu\dot{\gamma}$. The Bingham number is an indicator of the ratio of the constant to the variable component. Thus, the larger Bn the smaller the variation of τ and of the resulting force during the shaft motion. Hence, the circular shape of the force vs. displacement cycle in the Newtonian case tends to a rectangular one as the Bingham number is increased. Of course, the force also has a pressure component, but the momentum equation suggests that pressure forces behave similarly to viscoplastic ones when Re^* is small. These theoretical findings are confirmed experimentally, see e.g. [14,41]. In fact, force-displacement diagrams for varying Bingham numbers can be found in most ER and MR damper studies, as they are obtained for different strengths of the electric or magnetic fields. However, usually it is the dimensional forces that are plotted, under the same scale, and since even at low field strengths the Bingham number is rather high, it is difficult to discern the differences in the curvature of the plots (for example, in Fig. 7(a) the differences between the curves for $Bn = 20$, 80 and 320 would not be easily discernable had the dimensional forces been plotted instead).

Fig. 7 (b) and (c) shows the viscoplastic and pressure contributions to the total force. In Fig. 7(b) the force that would result had there been no bulge is also plotted with dashed lines. It can be seen that the presence of the bulge increases the viscoplastic force only slightly. On the other hand, the pressure force is due solely to the bulge; in its absence there is no pressure force in the x-direction, since the projection of the shaft's surface in that direction is zero. Fig. 7(c) shows that the pressure force, normalised by F_{ref}, is almost independent of the Bingham number, having a value of about 0.7. This will be shown later to depend on the damper geometry. The viscoplastic force on the other hand does depend on Bn for lower values of Bn, but tends to unity as Bn is increased. The pressure forces appear rather small compared to the viscoplastic forces, but become more important as the Bingham number is increased. This implies also that the role of the bulge becomes more important as Bn is increased; however, as noted, asymptotically as Bn is increased, the ratio of viscoplastic to pressure forces tends to a certain limit.

It is interesting to examine what happens when the shaft reaches an extreme position and momentarily stops ($x = \pm\alpha$, shaft velocity $= 0$). It is most clearly seen in Fig. 7(d) that in the Newtonian case the fluid continues to flow, resulting in a non-zero reaction force, but in all the viscoplastic cases shown the fluid

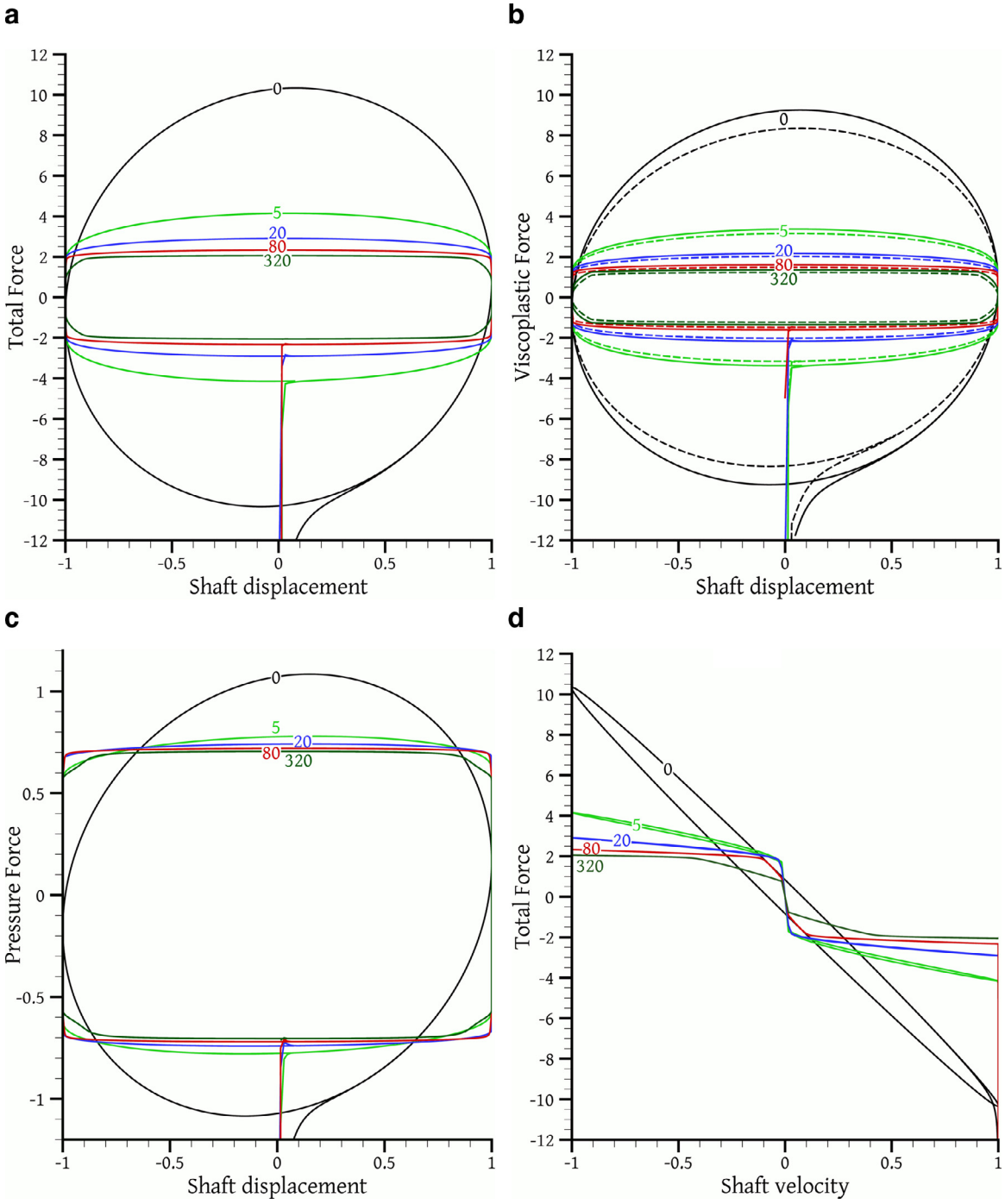

Fig. 7. Various components of force as a function of either shaft displacement or shaft velocity, for several different Bingham numbers which are indicated on each curve. Forces are dedimensionalised by F_{ref}, displacement by the oscillation amplitude α, and velocity by U. The dimensional parameters of each experiment are as shown in Table 1, except that the yield stress τ_y has been adjusted to obtain the Bingham numbers shown. All simulations have a duration of one period T, except the Newtonian case which has a duration of $2T$. Each curve is traversed in a counterclockwise sense with respect to time. In (b), the dashed lines indicate the force in the absence of a bulge.

stops (actually it becomes completely unyielded) and the reaction force F_R becomes zero. Nevertheless, even the slightest shaft motion causes non-zero rates of deformation and therefore yielding of the fluid, with the stress magnitude jumping from zero to the yield stress. Thus the force also immediately jumps from zero to some non-zero value, and then gradually increases further as the rate of deformation increases due to shaft acceleration. A departure from this behaviour can be noticed for the $Bn = 320$ case both in Fig. 7(d) and in Fig. 7(a), where a relatively smaller jump in F_R occurs relative to the smaller Bn cases, followed by a more gradual increase of F_R until it reaches a nearly constant value. This is due to the Navier slip boundary condition and will be explained in the following subsection.

Another interesting quantity that would help shed more light on the damper operation is the rate of dissipation of mechanical energy to thermal energy inside the fluid. For generalised Newtonian fluids, this rate, per unit volume, is given by the dissipation function

$$\phi \equiv \underline{\tau} : \nabla \underline{u} = \eta \dot{\gamma}^2 \tag{16}$$

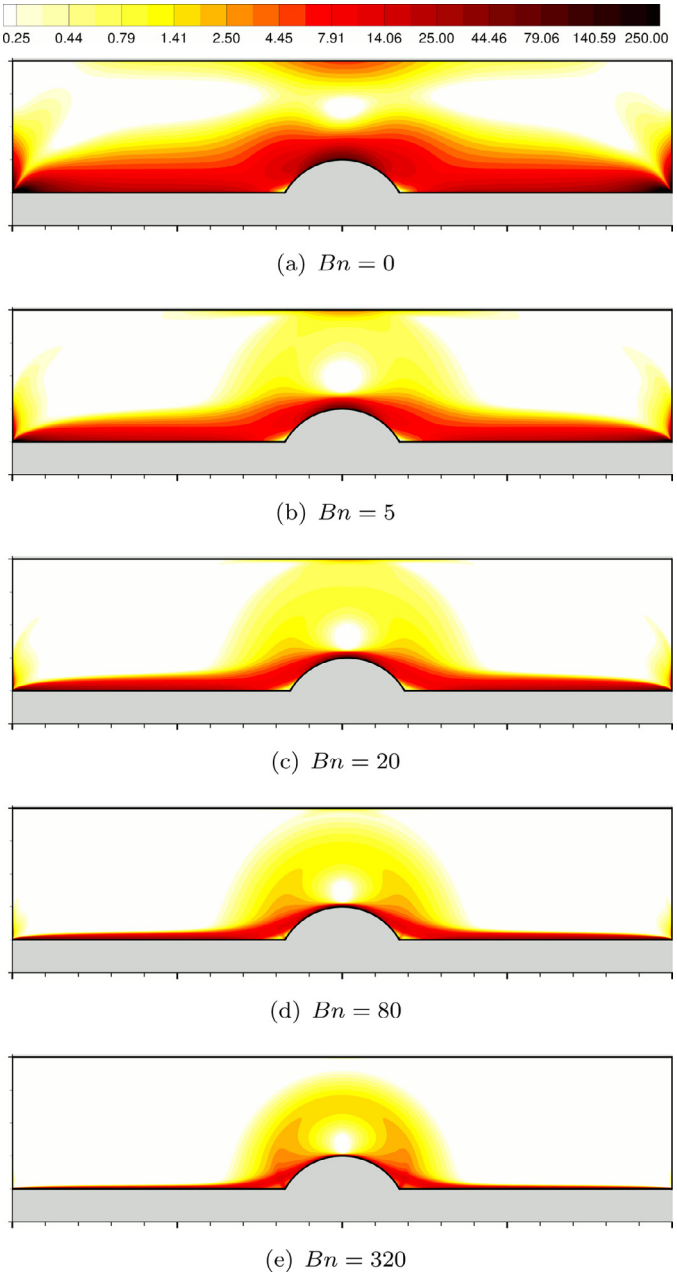

Fig. 8. Plots of the dimensionless dissipation function $\tilde{\phi} = \phi/\phi_{\text{ref}}$ (Eq. (16)) for the test cases of Fig. 7, at $t = T/2$.

The second equality is valid for generalised Newtonian fluids, for which $\underline{\underline{\tau}} = \eta\underline{\underline{\dot{\gamma}}}$. The term $\underline{\underline{\tau}} : \nabla \underline{u}$ gives the rate of work done in deforming the fluid, per unit volume. For viscoelastic fluids, some of this work is stored as elastic energy in the material, but for generalised Newtonian fluids, including the Bingham material considered here, this work concerns only conversion of mechanical energy into heat [63]. The dissipation function is dedimensionalised here by

$$\phi_{\text{ref}} = \tau_{\text{ref}} U/H = \tau_y \frac{U}{H} + \mu \frac{U^2}{H^2} \tag{17}$$

Fig. 8 shows plots of the dissipation function for the various cases, at a time instance when the shaft velocity is maximum. It is evident that as the viscoplasticity of the material increases, energy dissipation becomes more localised, confined to a thin layer of fluid surrounding the shaft and to a ring of rotating fluid between the bulge and the outer cylinder. The maximum energy dissipation appears to occur at the endpoints of the shaft, where it meets the outer damper casing, and at the top of the bulge. For low Bingham numbers, the energy dissipation at the shaft endpoints is very significant, and it is due to the very large velocity gradients there, despite the Navier slip boundary condition. At higher Bingham numbers the contribution of these areas to the overall energy dissipation diminishes – see also Fig. 4. The ring of material that rotates between the bulge and the outer cylinder also decreases in size as the yield stress is increased. For $Bn = 80$ (Fig. 8(d)) and 320 (Fig. 8(e)) the ring does not extend all the way up to the outer cylinder. This suggests that for these and higher Bingham numbers the chosen radius R_o of the enclosing cylinder has a negligible effect on the produced force, and that using a larger radius would not change the magnitude of the reaction force.

4.2. Effect of slip

In the next series of simulations we start from the base case (Table 1) and change the slip coefficient β. The only dimensionless number affected is $\tilde{\beta}$. Fig. 9 shows how the force $\tilde{F}_R$ and its components vary with the shaft displacement or velocity, for various values of this coefficient. As expected, increasing the slip coefficient decreases the reaction force and its components. Note that since the reference force F_{ref} used for the dedimensionalisation does not depend on the slip coefficient, the forces in the diagrams of Fig. 9 are directly comparable, unlike those of Fig. 7. All graphs in Fig. 9 show that the forces resulting from $\tilde{\beta} = 0.025$ (the base case) and $\tilde{\beta} = 0.00625$ are nearly identical. This suggests that for the base case, the slip coefficient is too small for the slip to have a significant impact on the flow. But for larger slip coefficients the flow is affected significantly.

We first turn our attention to Fig. 9(d) which refers to a bulgeless configuration and shows how the force varies with respect to shaft velocity (in the absence of a bulge the total force is equal to the viscoplastic force). For low $\tilde{\beta}$ the force behaves as expected: When the shaft velocity is zero, all of the material is unyielded and the force is also zero; then, the slightest movement of the shaft causes fluid deformation and therefore yielding and the stress jumps to τ_y, resulting in a sharp rise of the reaction force to $\tilde{F}_R \approx 1$. From that point on, $\tilde{F}_R$ continues to rise more slowly as the shaft velocity increases and so does the component of stress that is proportional to fluid deformation. Actually, the increase of force when the shaft starts to move is very sharp but not completely vertical. Of course, this could be attributed to regularisation (13), but one cannot help but notice that this force increase becomes much more gradual as $\tilde{\beta}$ is increased. The explanation lies in the Navier slip boundary condition (10). Taking a closer look at what happens when the shaft starts to move from a still position, we note that initially the material is completely unyielded. Suppose that after a small time the shaft has acquired a small velocity $\tilde{u}_{sh}$. According to the Navier slip condition (10) this causes the shaft to impose a stress $\tilde{\tau} = \tilde{\beta}^{-1}(\tilde{u}_{sh} - \tilde{u}) \leq \tilde{\beta}^{-1}\tilde{u}_{sh}$ on the viscoplastic material. If this is smaller than the yield stress then the material will remain unyielded, and thus motionless. The shaft then simply slides over the motionless material without moving it, and the stress that develops in the shaft / material interface is due to the friction between them. Since the material is motionless, $\tilde{u} = 0$ and the boundary condition is $\tilde{\tau} = \tilde{\beta}^{-1}\tilde{u}_{sh}$. As the shaft accelerates and $\tilde{u}_{sh}$ increases, the stress $\tilde{\tau}$ also increases proportionally and eventually it reaches the yield stress $\tilde{\tau}_y = Bn/(Bn+1)$. This is the onset of yielding, and occurs at a critical shaft velocity of

$$\tilde{u}_{sh}^{y} = \tilde{\beta}\frac{Bn}{Bn+1} \tag{18}$$

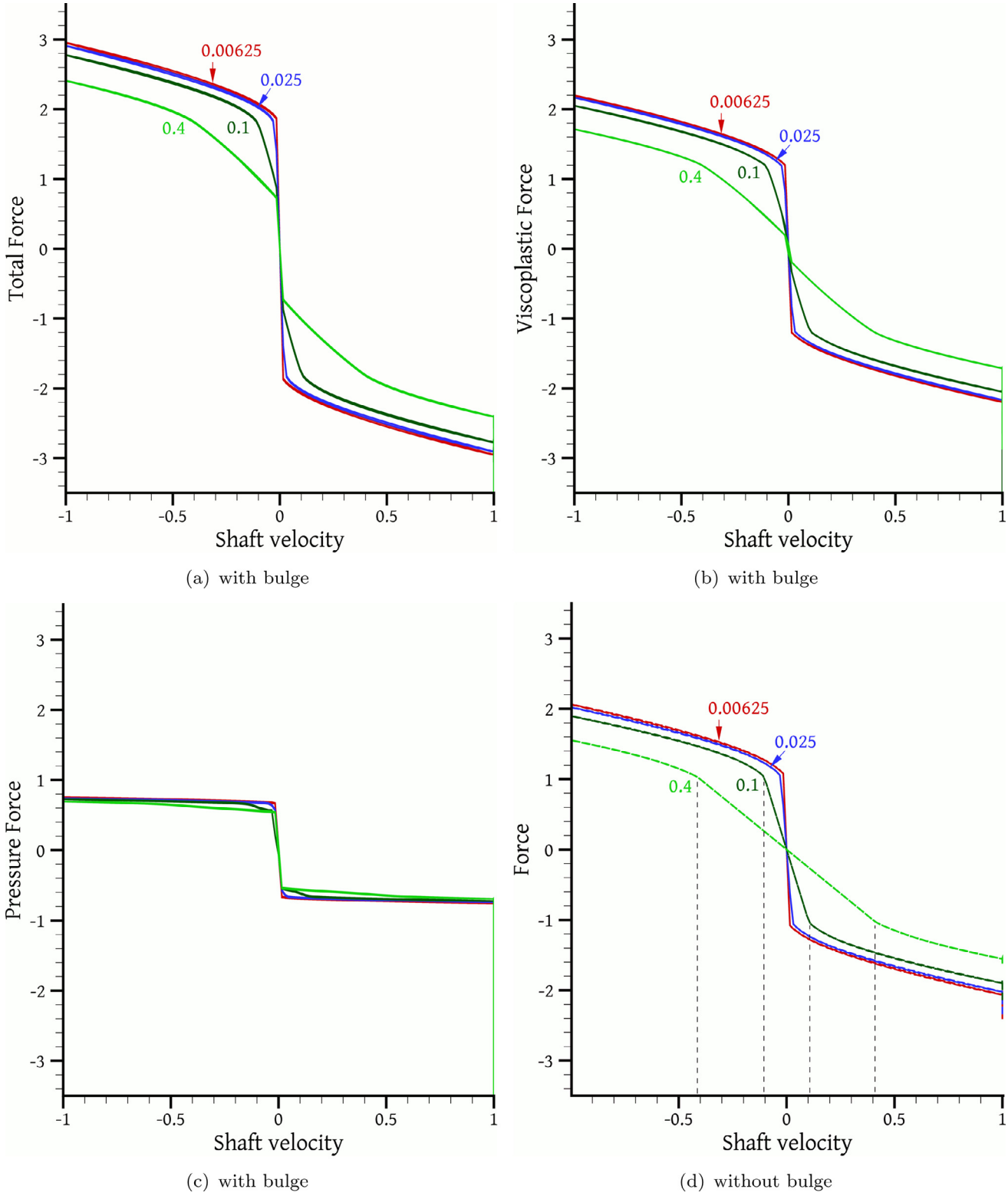

Fig. 9. Various force components as a function of shaft velocity, for different values of the dimensionless slip parameter $\tilde{\beta}$, indicated on each curve. Forces are dedimensionalised by F_{ref} and velocity by U. The dimensional parameters of each experiment are as shown in Table 1, except that the slip parameter β has been adjusted to obtain the indicated values of $\tilde{\beta}$. Each curve is traversed in a counterclockwise sense with respect to time. Fig. (d) refers to the viscous force in an experiment without a bulge (this is also the total force, because the pressure force is zero in this case).

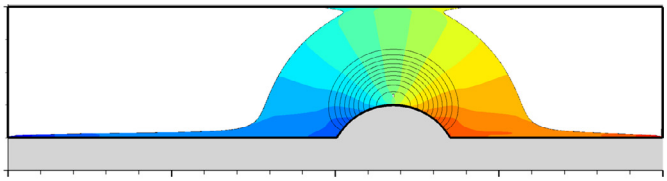

(a) $\tau_y = 31.4\text{Pa}$ ($Bn = 20$), $\beta = 7.619{\cdot}10^{-4}$ m/Pa·s ($\tilde{\beta} = 0.4$), $t = 0.7(T/4)$

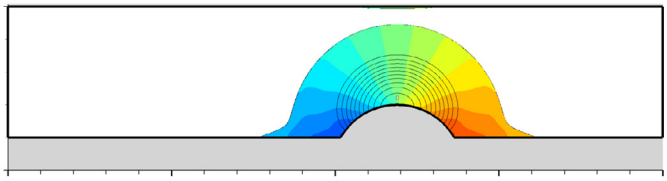

(b) Same as (a), but at $t = 0.8(T/4)$

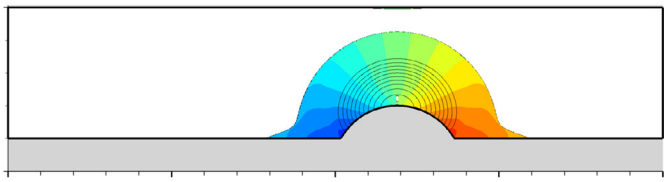

(c) $\tau_y = 502.7\text{Pa}$ ($Bn = 320$), $\beta = 4.762{\cdot}10^{-5}$ m/Pa·s ($\tilde{\beta} = 0.38$), $t = 0.8(T/4)$

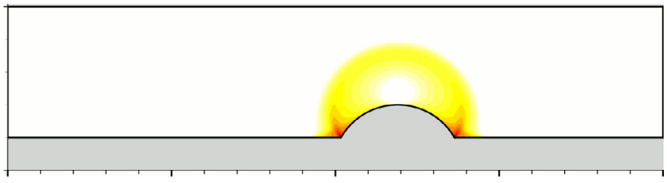

(d) Same as (c), but the dissipation rate is plotted

Fig. 10. Flow field snapshots at times when the wall stress is close to the yield stress of the material. The parameters of the problems are as in Table 1 unless otherwise indicated. Figures (a) and (b) correspond to the "$\tilde{\beta} = 0.4$" case of Fig. 9, while Figs. (c) and (d) correspond to the "$Bn = 320$" case of Fig. 7. See captions of Figs. 5 and 8 for visualisation details.

These theoretical results are confirmed by Fig. 9(d). Indeed, since $Bn/(Bn+1) \approx 1$ for $Bn = 20$, the material should yield when the shaft velocity has reached $\tilde{u}^y_{sh} \approx \tilde{\beta}$, i.e. $\tilde{u}^y_{sh} \approx 0.1$ for $\tilde{\beta} = 0.1$ and $\tilde{u}^y_{sh} \approx 0.4$ for $\tilde{\beta} = 0.4$. This is confirmed by Fig. 9(d). Furthermore, up to the yield point the dimensionless force should be proportional to $\tilde{\tau} = \tilde{\beta}^{-1}\tilde{u}_{sh}$, which is again confirmed by the linear variation of force in Fig. 9(d), for velocities of magnitude $|\tilde{u}_{sh}| \leq \tilde{u}^y_{sh}$. For shaft velocities larger than $\tilde{u}^y_{sh}$ the material yields so that the slip velocity $\tilde{u}_{sh} - \tilde{u}$ increases more slowly than before (as now $\tilde{u} \neq 0$), causing the slope of the force curves to decrease.

The existence of the bulge has the consequence that even the slightest shaft motion changes the domain shape and thus causes deformation and yielding of the material. Therefore, the only instance when the material may be completely unyielded is when the shaft velocity is zero. To see what happens, Fig. 10(a) and (b) shows snapshots of the flow field as the shaft is decelerating, at two time instances, when its velocity is just above $\tilde{u}^y_{sh}$ (Fig. 10(a)) and when it is just below $\tilde{u}^y_{sh}$ (Fig. 10(b)). In Fig. 10(a) the stress at the shaft / material interface is everywhere above the yield stress and the shaft is everywhere surrounded by a layer of yielded material. In Fig. 10(b) the stress at the shaft / material interface is mostly below the yield stress so that the shaft is in direct contact with, and sliding on, unyielded material over most of its length; however, the bulge is surrounded by a bubble of yielded material. The consequences of this on the force can be seen by comparing the $\tilde{\beta} = 0.4$ curves of Fig. 9(d) and (b); when there is a bulge, at the onset of shaft motion there is an immediate albeit relatively small increase in the force, contrary to the no-bulge case, due to yielding of the material surrounding the bulge. Thus, slip may obscure the viscoplastic nature of the material by causing apparent flow that hides the existence of a yield stress, but it cannot do so completely if the shaft has a bulge. Note that this phenomenon will occur for any finite value of the slip coefficient; it occurs also for $\tilde{\beta} = 0.00625$ and 0.025 in Fig. 9 only that it is difficult to discern because the corresponding values of $\tilde{u}^y_{sh}$ are very small. Slip is known to introduce such increased complexity to viscoplastic flows, see e.g. [39,64] for other examples. As far as the pressure force is concerned, Fig. 9(c) shows that it is relatively independent of the slip coefficient.

These phenomena become more pronounced not only when the slip coefficient is increased, but also when the yield stress is increased; in the latter case a higher shaft velocity is required for yielding to occur. This is reflected on the dimensionless slip coefficient, Eq. (11), which depends not only on β but also on Bn. Thus the slip phenomena are more pronounced for $Bn = 320$ in Fig. 7 than for lower Bn numbers. In fact the $Bn = 320$ case of Fig. 7 has $\tilde{\beta} = 0.38$ which is very close to the $\tilde{\beta} = 0.4$ case of Fig. 9, and so they have very similar yield shaft velocities $\tilde{u}^y_{sh}$. Fig. 10(c) shows a snapshot of the $Bn = 320$ case at the same time instance as for Fig. 10(b); the two flow fields can be seen to be very similar. Also, the dissipation function is plotted in Fig. 10(d) and, as expected, it can be seen to be non-zero only within the yielded "bubble" surrounding the bulge.

Other differences in the dissipation function distribution that are due to slip can be seen by comparing Figs. 11(a) and 11(b). Increasing slip can be seen to reduce energy dissipation in the bulk of the material, especially at the shaft ends and at the tip of the bulge, by relaxing the large velocity gradients there. The weakening of the flow also makes the effect of the outer cylinder weaker, with the ring of rotating material not extending up to the outer cylinder in Fig. 11(b). Finally, one can notice in Fig. 11(a) (and in other low slip cases) that there is some material trapped in the corners between the bulge and the shaft; but in Fig. 11(b) (and also in Fig. 8(e), where slip is again large) there is no such entrapment. This is reminiscent of the unyielded cups which are observed at the poles of a sphere falling through a viscoplastic material [65]; actually, Fig. 5 shows that the material at the bulge corners is yielded, but the low rates of deformation suggested there by Figs. 8 and 11 indicate that the material is close to the unyielded state. It would not be unreasonable to suspect that increasing the grid resolution locally might reveal small amounts of uyielded material at the corners.

Figs. 10 (d) and 11(b) do not show the whole picture as far as energy dissipation is concerned. The dissipation function only accounts for the mechanical energy that is converted into heat due to fluid deformation. But, whenever there is slip, mechanical energy is also converted into heat by the sliding friction between the shaft and the material. Fig. 12 shows two curves on each plot: the rate of work done by the shaft and the rate of energy dissipation within the material. The area between the two curves is the energy converted to heat due to sliding friction. When the slip coefficient is small, almost all of the energy is dissipated within the bulk of the material due to fluid deformation, and the sliding friction plays a very minor role. On the contrary, when the slip coefficient is large, sliding friction plays a crucial role, converting mechanical energy into heat directly on the fluid / shaft interface, whereas energy dissipation in the bulk of the material is weak. In Fig. 12(f), which corresponds to a bulgeless shaft, the energy dissipation in the bulk

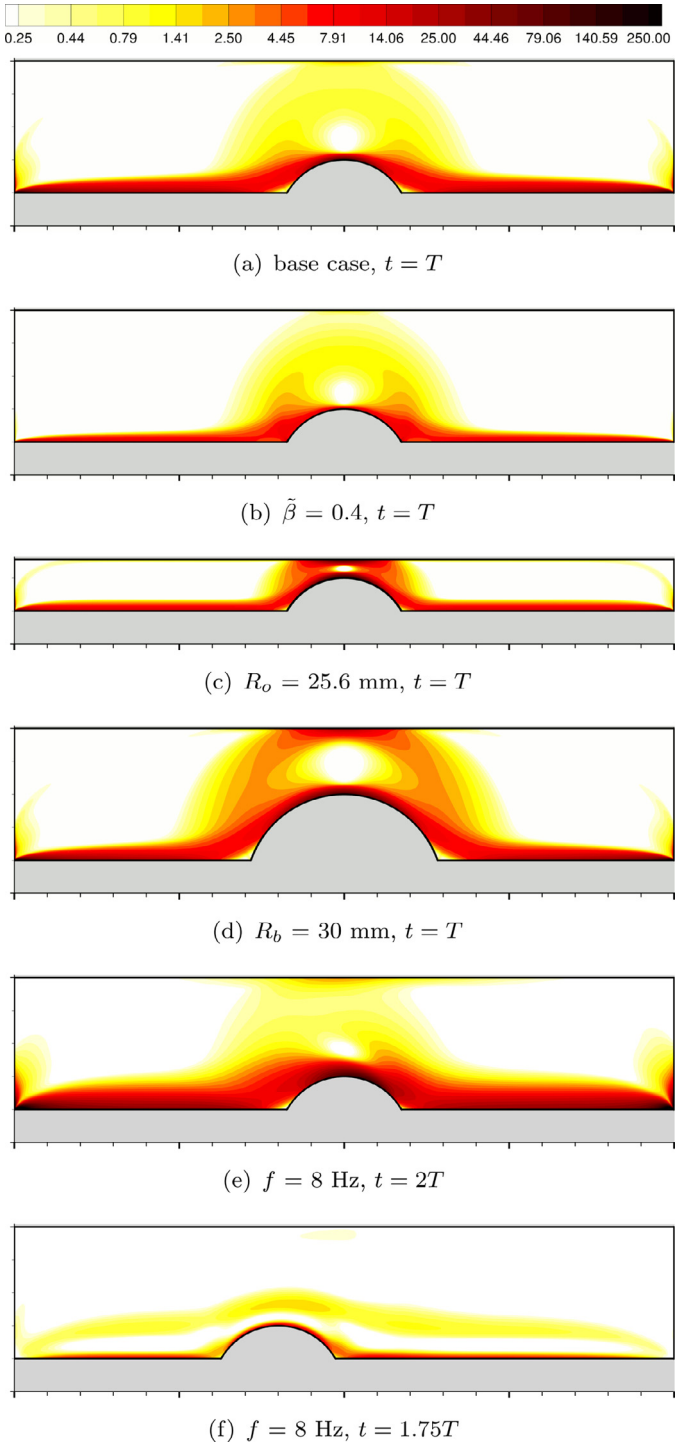

Fig. 11. Plots of the dimensionless dissipation function $\tilde{\phi} = \phi/\phi_{\text{ref}}$ (Eq. (17)) for various cases. The dimensional parameters have the values listed in Table 1, unless otherwise indicated in each figure caption.

of the material (red line) is zero over the time intervals during which the material is completely unyielded ($u_{sh} < u_{sh}^y$). On the contrary, in Fig. 12(c) (bulged shaft) this is never zero except when the shaft is stopped, as otherwise the bulge always causes some yielding, as discussed previously. We note, finally, that Fig. 12(a) and (d) provide further evidence that the flow is in quasi steady state, since all the instantaneous shaft work is dissipated, eventually by viscous forces. The work done in accelerating the fluid, i.e. increasing its kinetic energy, is negligible. This shows that the inertia of the system is negligible as well. Cases with increased significance of inertia will be examined later.

4.3. Effect of the damper geometry

The effect of the bore radius R_o on the reaction force is illustrated in Fig. 13. The radii selected are 50 (base case), 37.15, 29.8 and 25.6 mm, while the rest of the dimensional parameters have the values displayed in Table 1. The selected values of R_o are such that the length of the gap $R_o - R_b$ decreases by a constant ratio of 1.75. Since lengths are dedimensionalised by $H = R_o - R_i$, changing R_o affects all the dimensionless parameters. In particular, compared to the base case of $R_o = 50$ mm, in the $R_o = 25.6$ mm case Bn has fallen from 20 to 7.8, Re^* has fallen from 0.12 to 0.11 (but Re has fallen from 2.51 to 0.98), Sr has increased from 3.14 to 8.05, and $\tilde{\beta}$ has increased slightly from 0.025 to 0.027. Therefore, judging from these numbers, reducing the bore radius in the present configuration should in general reduce the viscoplasticity of the flow and also mildly reduce its inertial character.

We first examine the case where the shaft has no bulge. Fig. 13 includes results for bulgeless shafts, drawn in dashed lines, for all the selected R_o values. This is hard to see in the Figure though, because all the dashed curves nearly coincide. Therefore, for the range of values considered, the normalised force $\tilde{F}_R$ is nearly independent of R_o in the absence of a bulge; the actual force F_R increases slightly because $\tilde{F}_R$ is normalised by F_{ref} which is proportional to $\tau_{\text{ref}} = \tau_y + \mu U/H$, which increases from about 33 Pa at $R_o = 50$ mm to about 35.5 Pa at $R_o = 25.6$ mm. However, if Bn is an appropriate indicator of the viscoplasticity of the flow, one would expect a greater difference between the force curve for $R_o = 50$ mm ($Bn = 20$) and that for $R_o = 25.6$ mm ($Bn = 7.8$) – compare for example the curves for $Bn = 20$ and $Bn = 5$ in Fig. 7(b). As it is easily deduced from Figs. 14(a) and 6(d), despite the Bingham number being lower, a larger percentage of the material is unyielded when $R_o = 25.6$ mm than when $R_o = 50$ mm. This can be attributed to the geometrical confinement of the former case, which forces the streamlines to be straight over a longer distance, thus reducing the deformation rates and favouring the unyielded state.

In order to obtain more insight, we find it useful to discuss a one-dimensional flow that shares some similarity with the present flow, that of annular Couette flow where the inner cylinder moves with a constant velocity and the outer one is stationary. This flow is described in the Appendix, where it is shown that the outer radius R_o is important only if the flow is completely yielded, which occurs if R_o does not exceed a critical value R_y (given by Eq. (A.7) in the Appendix), that depends on the dimensionless number

$$B = \frac{\tau_y R_i}{\mu U} \tag{19}$$

(an alternative definition of the Bingham number, depending only on R_i and not on R_o). If R_o exceeds R_y then the material from R_i to R_y is yielded with its velocity independent of R_o, and from R_y to R_o it is unyielded with zero velocity. Thus in this case it would be misleading to use the Bingham number Bn as an indicator about the flow; the alternative Bingham number B conveys all the relevant information (Eqs. (A.7), (A.8)).

Fig. 15 shows that something similar happens in the bulgeless damper cases, in the middle of the bore length. Fig. 15(a) shows that the velocity gradient at the inner cylinder, and therefore also the force F_R, is relatively independent of R_o; thus F_R is relatively insensitive to changes in Bn that are due to changes in R_o, as Figs. 13(a)–(b) also show. On the other hand, Fig. 15(b) shows that the velocity gradient at the inner cylinder, and therefore also the force, depends strongly on τ_y; thus F_R is sensitive to changes in

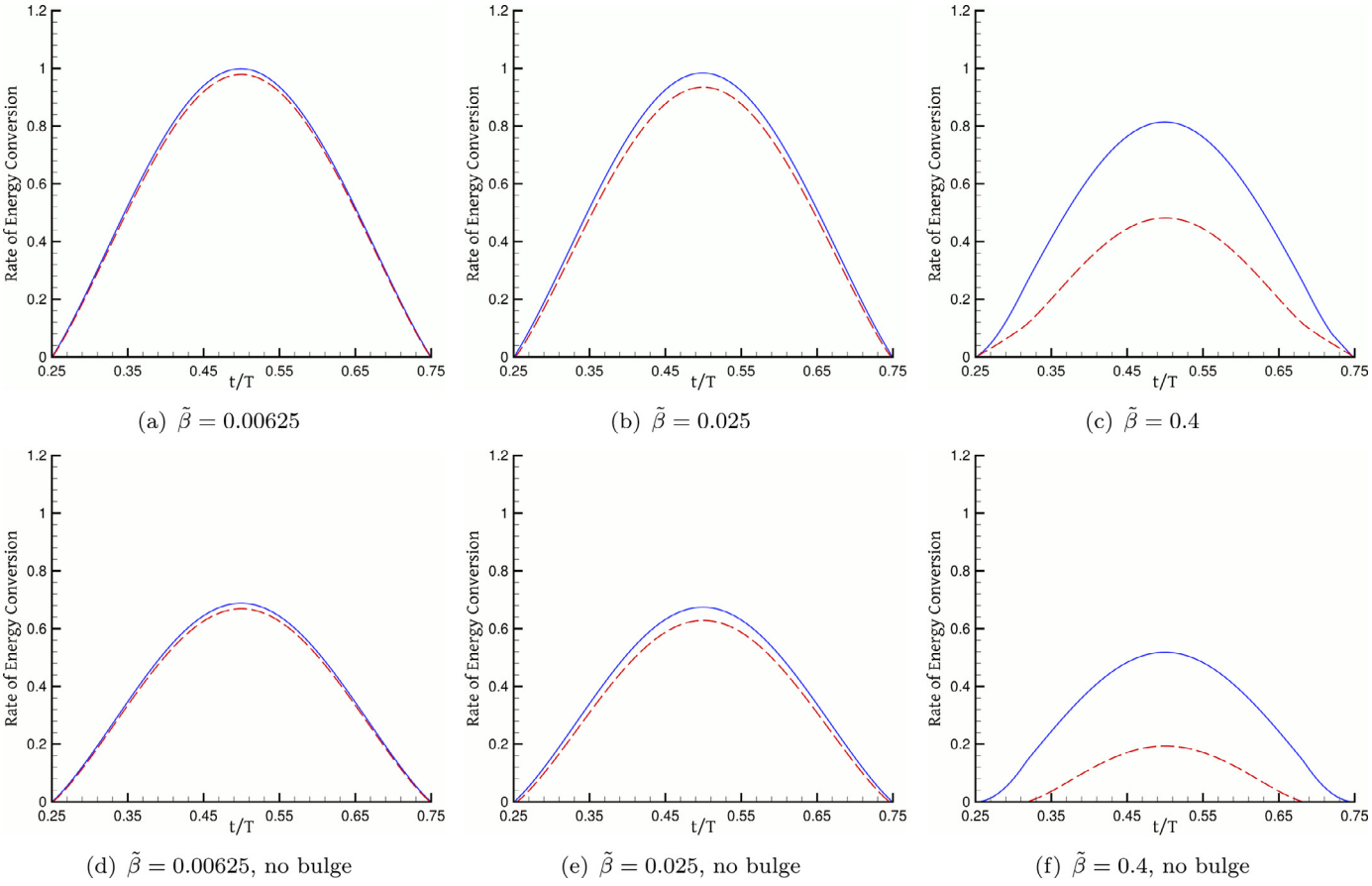

Fig. 12. Rate of energy dissipation for various values of the dimensionless slip coefficient $\tilde{\beta}$, with (top) and without (bottom) a bulge. The continuous blue line is the instantaneous total power consumption of the damper, calculated as $-F_k u_{sh}$. The dashed red line is the rate of dissipation of mechanical energy into heat due to fluid deformation, i.e. the integral of the dissipation function (16) over the computational domain. Both the power consumption and the dissipation rate are normalised by $\phi_{\text{ref}}\Omega_{\text{tot}}$ where Ω_{tot} is the total volume occupied by the fluid and ϕ_{ref} is defined by Eq. (17). The flow parameters are as listed in Table 1, except for the slip coefficient which is varied to obtain the values of $\tilde{\beta}$ shown. (For interpretation of the references to colour in this figure legend, the reader is referred to the web version of this article).

Bn that are caused by changes in τ_y, as shown in Fig. 7(b). So, one must be careful when using *Bn* to assess the viscoplasticity of the flow. Fig. 15 includes the corresponding yield lines for annular Couette flow (dash-dot lines). Obviously, there are differences from the damper cases, but the trends are similar: R_o has a minimal effect on the yield surfaces, while the effect of τ_y is much more important.

A one-dimensional flow that is even closer, although not as enlightening, is annular Couette–Poiseuille flow in which the pressure gradient is precisely that which results in zero overall flow between the two cylinders. The equations are given again in the Appendix, and the velocity profiles are drawn in dashed lines in Fig. 15. The similarity with the annular cavity flow is striking; the profiles are nearly identical, and any differences can be attributed to the boundary conditions: for annular Couette–Poiseuille flow we used no-slip conditions. This explains why the discrepancy becomes larger with the Bingham number, since viscoplasticity leads to more slip as was discussed earlier. It is expected that annular Couette–Poiseuille flow is a good approximation for annular cavity flow away from the cavity sides, especially for long cavities, when inertia effects are weak. This has not been investigated further, although it could be useful for certain practical applications.

In the case with a bulge, R_o has a significant impact, for the cases studied. It is evident from Fig. 13 that the narrower the cylinder, the greater the force, and the less "viscoplastic" (flat) the shape of its graph. An explanation can be sketched with the help of Fig. 14. As the gap between the bulge and the outer cylinder becomes narrower, larger fluid deformations and shear stresses develop there. This causes a moderate increase in the total viscoplastic component of F_R, as seen in Fig. 13(b), because the extent of this high-shear area is rather small. However, these high localised stresses make it more difficult for the material to flow through the constriction, and this requires higher pressure gradients to push it through. This is evident by comparing Fig. 14(c) and (d). The increased pressure gradient does not just have a localised effect, but it increases the pressure differences across the whole bulge resulting in a significant increase of the pressure force (Fig. 13(c)). Also, since the pressure gradient has to counteract the viscous stresses that oppose the fluid flow through the constriction, and the latter have a large $\mu\dot{\gamma}$ component (compared to their τ_y component) due to the narrowness of the constriction, the resulting pressure force is more proportional to the shaft velocity (more "Newtonian-like") the narrower the constriction is (again, see Fig. 13(c)).

In another set of simulations, the bore radius R_o is held constant while the bulge radius R_b is varied. This also has the effect of varying the narrowness of the constriction, but without changing any of the dimensionless numbers characterising the flow, except the geometric ratio R_b/R_o (Table 1). Fig. 16 shows that again, like when R_o was varied, constricting the stenosis increases F_R and it does so mostly through the pressure component. The explanation is the same as for the variation of R_o. It is interesting to note in Fig. 16(a) and (c) that some hysteresis is exhibited for

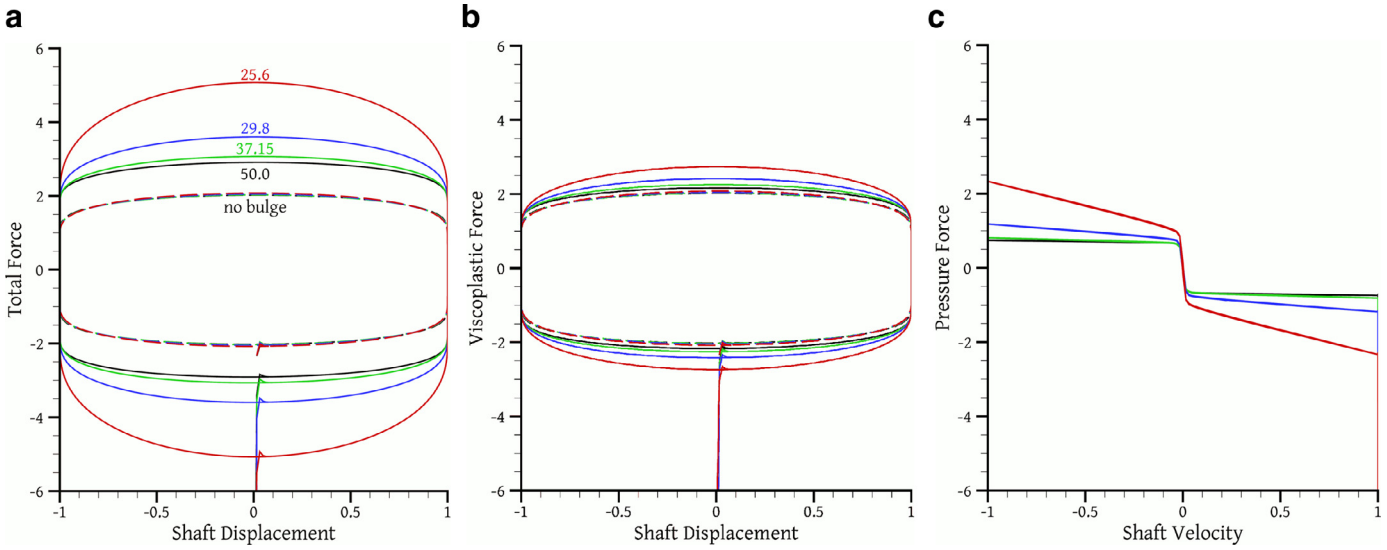

Fig. 13. The dimensionless reaction force and its components as a function of dimensionless shaft displacement or velocity, for various bore radii, R_o = 50, 37.15, 29.8 and 25.6 mm. The rest of the parameters are as listed in Table 1. In (a) and (b) the dashed lines depict results for bulgeless shafts.

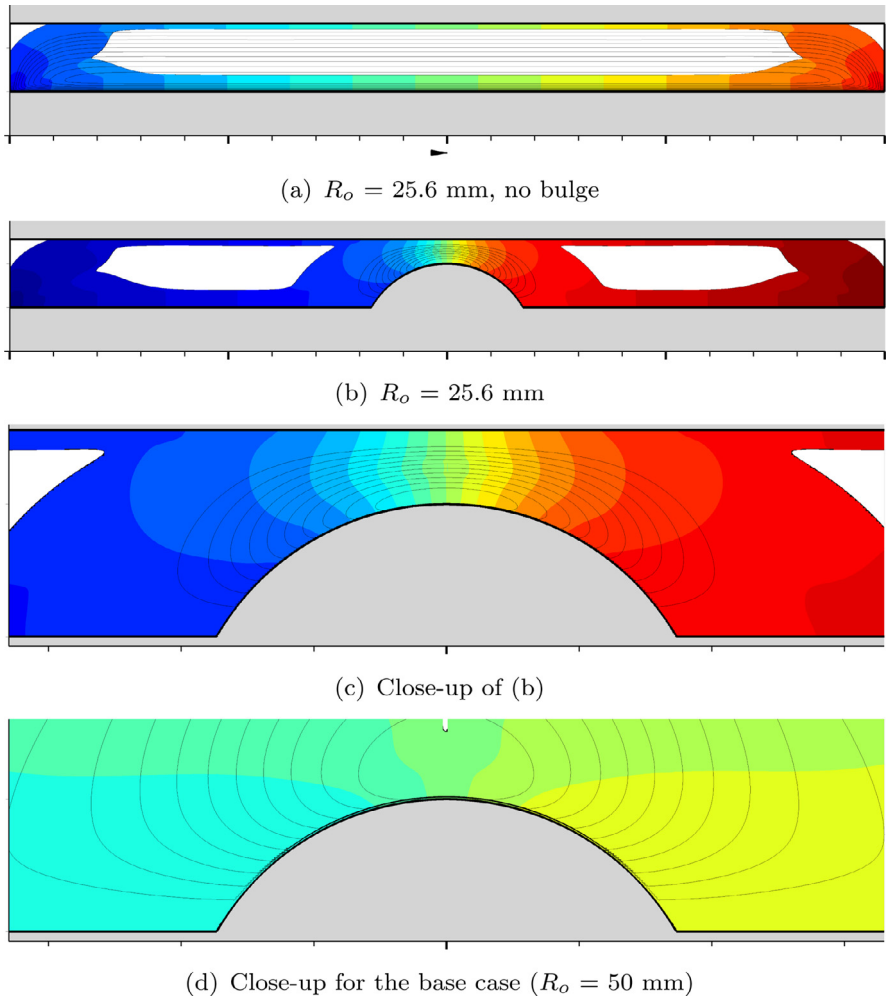

Fig. 14. Comparison between the flow fields for R_o = 25.6 mm and 50 mm (the base case), at $t = T$. The rest of the parameters are as listed in Table 1. The flow is visualised as described in the caption of Fig. 5, only that the dimensionless pressure contours have a step of 2.4.

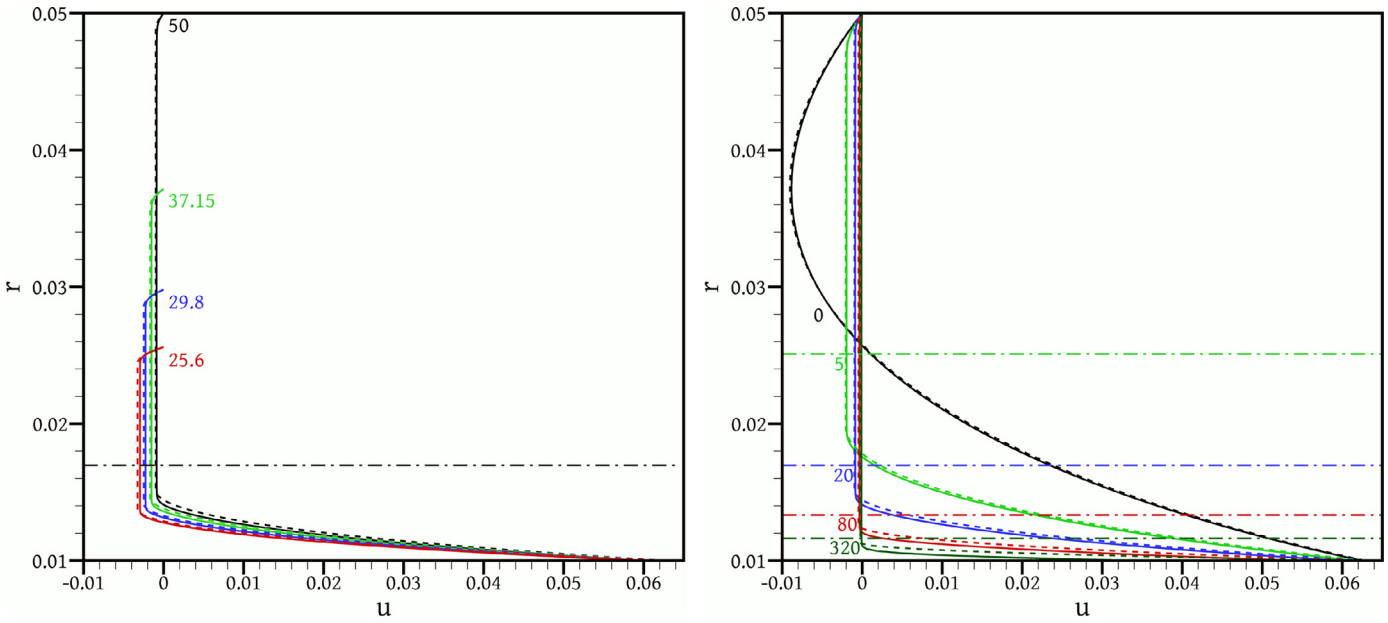

(a) Profiles for various R_o (mm) (b) Profiles for various Bn

Fig. 15. Solid lines depict profiles of the axial velocity u along the radial direction, at $x = L/2$ and $t = T$ ($t = 2T$ in the Newtonian case), for bulgeless shafts. Dashed lines depict the corresponding profiles for steady annular Couette–Poiseuille flow with zero net flow (see Appendix), of the same R_i, R_o, U τ_y and μ as the corresponding damper cases. Dash-dot lines are the yield lines of corresponding steady annular Couette flow (again, see Appendix), calculated from Eq. (A.7). In (a) profiles are shown for various values of R_o, while the rest of the dimensional parameters have the values shown in Table 1; there is only one dash-dot line because it is independent of R_o. In (b) profiles are shown for various values of Bn, obtained by varying τ_y and keeping the rest of the dimensional parameters as listed in Table 1.

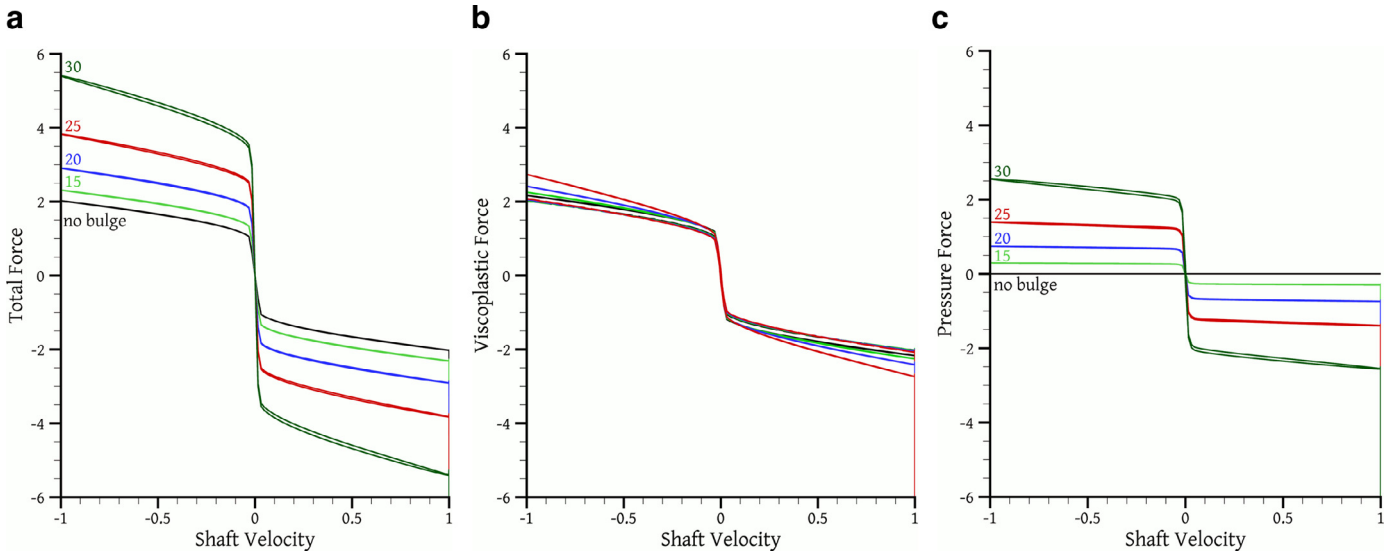

Fig. 16. The dimensionless reaction force and its components as a function of dimensionless shaft displacement or velocity, for various bulge radii, $R_b = 0$ (no bulge), 15, 20, 25 and 30 mm. The rest of the parameters are as listed in Table 1.

$R_b = 30$ mm, meaning that the relative magnitude of inertia forces increases with R_b, despite the Reynolds number being constant. Fig. 17 helps to explain why: increasing R_b results in increased velocities in a larger part of the domain as the constriction becomes narrower but also the bulge occupies a larger part of the axial extent of the shaft. The increased velocities imply increased velocity variations in time and space, and therefore increased inertia forces, as the flow is transient and the streamlines are curved.

Fig. 11 (c) and (d) shows plots of the dissipation function when the shaft velocity is maximum, for the cases of minimum bore radius and maximum bulge radius tested. In 11(c) one can discern very high dissipation rates also at the cylinder bore, opposite to the bulge. In 11(d) the rate of dissipation does not reach so high values near the bore, because the gap between the bulge and the bore is wider than in 11(c), but there is extensive energy dissipation in a wide area of the domain.

The results of this paragraph show that when changing the damper geometry it is important not to rely too much on what happens to the Bingham and Reynolds numbers in order to make conjectures about the effects of the geometry change on the viscoplastic and inertial character of the flow.

4.4. Effect of the frequency

Finally, we study the effect of the oscillation frequency on the damper response. In particular, in addition to the $f = 0.5$ Hz

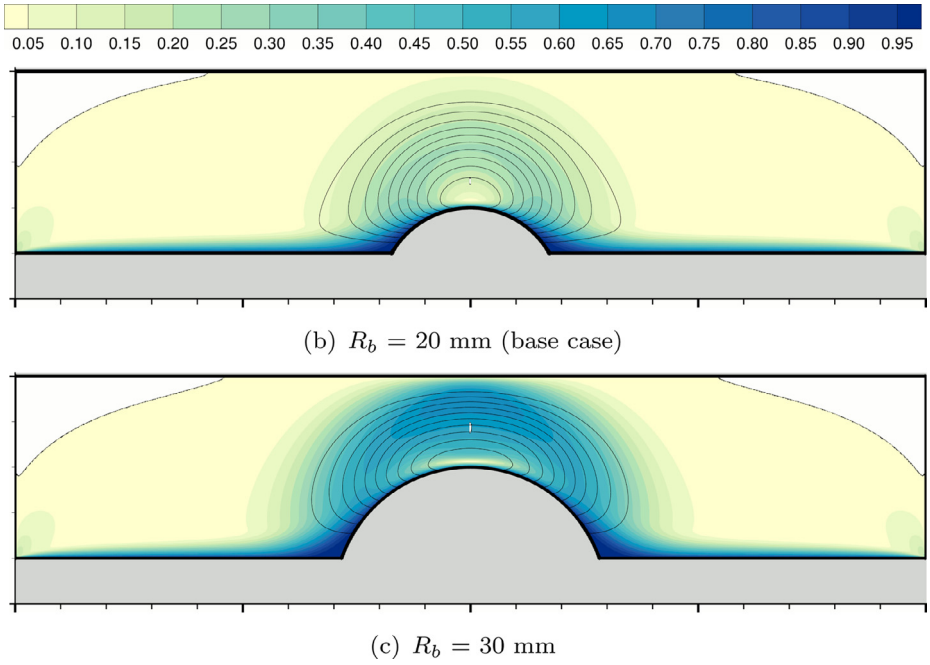

Fig. 17. Non-dimensional velocity magnitude $\| \underline{u} \|/U$ at $t = T$ for two different bulge radii R_b. The rest of the flow parameters are as listed in Table 1. Unyielded material is shown in white. The streamlines drawn correspond to equispaced values of the streamfunction from zero to the maximum value of each case.

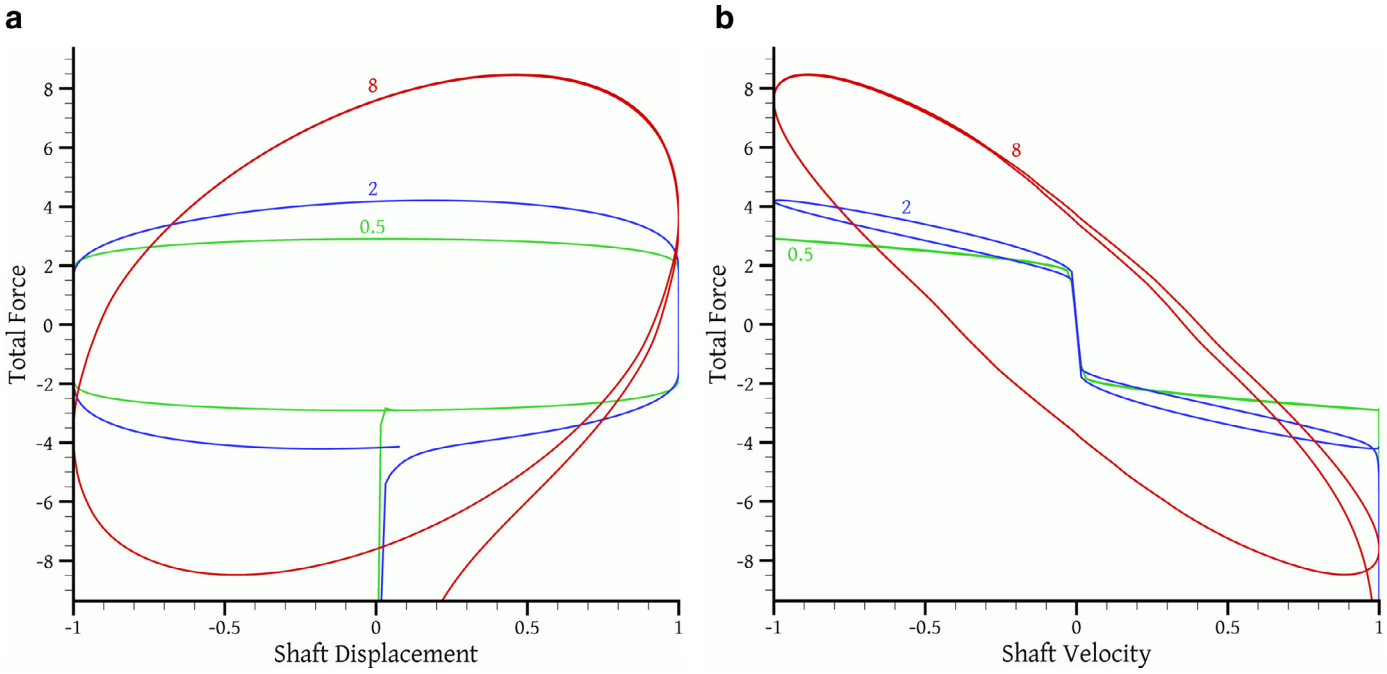

Fig. 18. The dimensionless reaction force as a function of dimensionless shaft displacement and velocity, for various oscillation frequencies, $f = 0.5$ (base case), 2 and 8 Hz. The rest of the parameters are as listed in Table 1.

base case, we performed simulations for $f = 2$ and 8 Hz, while keeping the rest of the dimensional parameters of Table 1 unaltered. The variation of the reaction force F_R with respect to shaft displacement and velocity is plotted in Fig. 18. For $f = 2$ Hz it was observed that all the material became unyielded when the shaft stopped, and so the simulation duration was set to $t \in [0, T]$, like for most other simulations; but for $t = 8$ Hz the material continues to flow even at the instances when the shaft is still, and so the simulation duration was extended to $t \in [0, 2T]$, which, as the results show (Fig. 18(a)), is more than enough to attain the periodic state.

Increasing the frequency while holding the amplitude of oscillation constant means that the maximum velocity U is increased proportionally. This results in a reduction of the Bingham number Bn and in an increase of the Reynolds number Re^*. Unlike the situation presented in Section 4.3, now the geometrical parameters of the problem do not change between the different frequency cases studied, and therefore Bn and Re^* are appropriate indicators

of the viscoplastic and inertial character of the flow, respectively. As far as the rest of the dimensionless numbers are concerned, the Strouhal number, being proportional to the dimensionless amplitude of oscillation, is not affected, while the slip coefficient $\tilde{\beta}$ drops, approaching its Newtonian value $\beta\mu/H$.

Evidently, as f increases, the invariability of the reaction force, which is characteristic of viscoplasticity, is lost. Fig. 18(b) shows that the relationship between F_R and the shaft velocity becomes more linear as f increases, a sign that the $\mu\dot{\gamma}$ component of stress becomes dominant over the τ_y component. This is reflected in the reduction of the Bingham number, which falls from 20 at $f =$ 0.5 Hz, to 5 at $f = 2$ Hz, and to 1.25 at $f = 8$ Hz.

Similarly, the skewness of the force curve for $f = 8$ Hz in Fig. 18(a) and the hysteresis of the corresponding curve in Fig. 18(b) reveal that when f is increased inertia becomes more important. This is reflected in the increase of the Reynolds number Re^*, which increases from 0.12 at $f = 0.5$ Hz, to 1.68 at $f = 2$ Hz, and to 17.9 at $f = 8$ Hz. This is in agreement with previous studies [14,15]. We note that with the present modelling assumptions hysteresis is only associated with inertia effects. In the literature it is often reported that in ER/MR dampers hysteresis is exhibited also under low inertia conditions, when the displacement approaches its extreme values (e.g. [13,17,41,66]). It has been proposed that this is due to the fluid exhibiting pre-yield elastic behaviour [66] or to compressibility effects [13], neither of which are accounted for by the present Bingham model.

Fig. 19 shows the time history of the rate of energy absorption by the damper, $-F_R u_{sh}$, together with the rate of energy dissipation in the bulk of the material due to its deformation, calculated as the integral of the dissipation function, for $f = 2$ and 8 Hz. The corresponding plot for $f = 0.5$ Hz is shown in Fig. 12(b). Obviously, as the frequency increases, there develops a phase difference between the total rate of energy absorption and the rate of energy dissipation due to fluid deformation. In Fig. 12(b) they are in phase with each other and with the shaft velocity. However, in Fig. 19(a), and even more so in Fig. 19(b), the variation of the total rate of energy absorption is shifted towards earlier times, while the dissipation due to fluid deformation remains in phase with the shaft velocity. This can be attributed to the role of inertia, which becomes more important when the frequency is increased. In what follows, a simple explanation for this will be presented which results in an algebraic formula that describes well the main characteristics of the damper response.

Taking the dot product of the velocity vector with the momentum equation and integrating over the whole volume Ω of the viscoplastic material, one obtains, after some manipulation, an energy balance for the whole of that material [63]:

$$\underbrace{\int_{\partial\Omega}\left(-p\underline{n}\cdot\underline{u}+\underline{n}\cdot\underline{\underline{\tau}}\cdot\underline{u}\right)\mathrm{d}A}_{\substack{\text{Rate of work done by external forces}\\ =-F_R u_{sh}}} = \underbrace{\int_{\Omega}\underline{\underline{\tau}}:\nabla\underline{u}\,\mathrm{d}\Omega}_{\substack{\text{Rate of energy dissipation}\\ \text{due to fluid deformation}}} + \underbrace{\int_{\Omega}\rho\underline{u}\cdot\frac{\mathrm{D}\underline{u}}{\mathrm{D}t}\,\mathrm{d}\Omega}_{\substack{\text{Rate of increase of the}\\ \text{kinetic energy of the fluid}}} \tag{20}$$

where $\partial\Omega$ is the boundary of the material, consisting of its interface with the shaft and the containing cylinder. The vector $\underline{n}$ is the outward unit vector normal to this surface, $\mathrm{d}A$ is an infinitesimal area of the surface, and $\mathrm{D}/\mathrm{D}t = \partial/\partial t + \underline{u}\cdot\nabla$ is the substantial time derivative. The above equation says that all the work done on the fluid by the motion of the shaft is either dissipated or stored as kinetic energy of the fluid. Actually, the left hand side is only equal to $-F_R u_{sh}$ in the absence of slip; otherwise it is smaller. But for this simplified analysis we will neglect slip. The goal is to make conjectures about the temporal variation of the terms of the right-hand side of Eq. (20) and combine them to estimate the overall temporal variation of the damper work. To proceed, we will assume that the terms of the right-hand side can be expressed as products of a characteristic force, viscoplastic or inertial, respectively, times a characteristic fluid velocity.

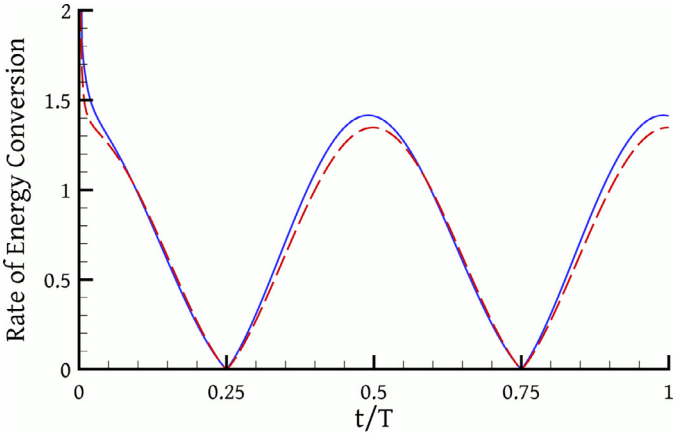

(a) $f = 2$ Hz

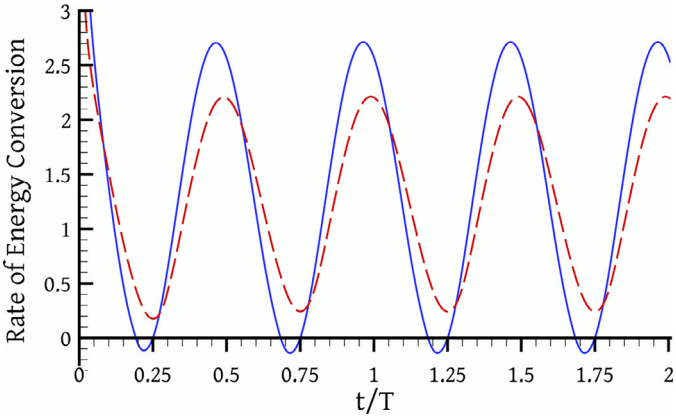

(b) $f = 8$ Hz

Fig. 19. Instantaneous power consumption of the damper (blue, solid line) and rate of energy dissipation due to fluid deformation (red, dashed line) for different oscillation frequencies. For details see the caption of Fig. 12. (For interpretation of the references to colour in this figure legend, the reader is referred to the web version of this article).

Velocities and velocity gradients in the fluid can be assumed to be roughly proportional to the shaft velocity $u_{sh} = U\cos(\omega t)$. Then, if the flow is viscoplastic, the viscoplastic forces would be expected to be of the form $F_V = F_V^0(b\,\mathrm{sign}(\cos(\omega t)) + \cos(\omega t))/(b+1)$, for some constant b proportional to the Bingham number. But the function $b\,\mathrm{sign}(\cos(\omega t))$, which is a square wave of the same frequency as $\cos(\omega t)$, bears some resemblance to $\cos(\omega t)$ and their sum can be replaced by just $(b+1)\cos(\omega t)$ for the purposes of this simplified analysis. A typical viscoplastic force would then have the form $F_V = F_V^0\cos(\omega t)$. The maximum value F_V^0 would increase with the maximum shaft velocity $U = \alpha\omega$ but not proportionally, due to the constant plastic component of the force; but it should tend to become proportional to U (and ω) at high frequencies.

Similarly, we assume that accelerations in the fluid are proportional to the shaft acceleration, $\dot{u}_{sh} = -\omega U\sin(\omega t)$, so that a typical inertia force such as that appearing in the last term of Eq. (20) has the form $F_I = \rho\mathrm{D}\underline{u}/\mathrm{D}t = -F_I^0\sin(\omega t)$. The maximum value F_I^0 would be proportional to the maximum shaft acceleration $\omega U = \omega^2\alpha$. Thus, increasing the frequency favours inertial forces

over viscous forces: the ratio F_I^0/F_V^0 tends to become proportional to ω.

Under these assumptions Eq. (20) can be approximated by

$$\begin{aligned}
-F_R u_{sh} &= c\big(F_V^0\cos(\omega t) - F_I^0\sin(\omega t)\big)U\cos(\omega t)\\
&= \underbrace{cU\sqrt{(F_V^0)^2+(F_I^0)^2}}_{c'}\left(\frac{F_V^0}{\sqrt{(F_V^0)^2+(F_I^0)^2}}\cos(\omega t)\right.\\
&\quad\left.-\frac{F_I^0}{\sqrt{(F_V^0)^2+(F_I^0)^2}}\sin(\omega t)\right)\cos(\omega t)\\
&= c'(\cos\delta\cos(\omega t) - \sin\delta\sin(\omega t))\cos(\omega t)\\
&= c'\cos(\omega t+\delta)\cos(\omega t)\\
&= (c'/2)\left[\cos\delta + \cos(2\omega t+\delta)\right] \qquad (21)
\end{aligned}$$

where we have used some simple trigonometric identities, c and c' are constants (actually, c' depends on ω but not on t), and δ is the angle adjacent to the side of length F_V^0 of a right triangle whose perpendicular sides have lengths F_V^0 and F_I^0. Thus $\delta = \arctan(F_I^0/F_V^0)$, and when the viscous forces dominate ($F_I^0/F_V^0 \to 0$), i.e. when the Reynolds number is very small, then δ is close to zero; and when the inertia forces are much larger than the viscous forces ($F_I^0/F_V^0 \to \infty$), i.e. when the Reynolds number is very large, then δ tends to $\pi/2$.

According to Eq. (21), the rate of energy absorption by the damper is proportional to $\cos\delta + \cos(2\omega t+\delta)$; this has two parts: a constant part, $\cos\delta$, and a time-varying part, $\cos(2\omega+\delta)$. It follows that the rate of energy absorption by the damper varies with a frequency of 2ω, twice that of the shaft oscillation. This is confirmed by Figs. 12 and 19, and is easily explained by the fact that each shaft oscillation can be split into two half-periods, one when the shaft is moving from left to right and one when the shaft is moving from right to left. The variation of the rate of energy absorption is exactly the same in both half-periods, due to flow symmetry: $F_R(t+T/2)u_{sh}(t+T/2) = (-F_R(t))(-u_{sh}(t)) = F_R(t)u_{sh}(t)$. Therefore each of these two half-periods is a full period of the variation of the rate of energy absorption.

When Re^* is small and inertia is negligible then $\delta \approx 0$ and $\cos(\delta) \approx 1$ and Eq. (21) predicts that $-F_R u_{sh}$ is proportional to $1+\cos(2\omega)$, which is always positive or zero. This is confirmed by Figs. 12(b) and 19(a). It is also in phase with the shaft oscillation, albeit at twice the frequency; when the shaft moves with maximum velocity (either positive or negative) $-F_R u_{sh}$ is maximum, and when the shaft momentarily becomes still $-F_R u_{sh}$ drops to zero. This is because the only forces of importance are the viscous forces, and they are proportional to the shaft velocity, according to our assumptions. Fig. 12, corresponding to a low Reynolds number, confirms this.

On the other hand, if the relative magnitude of the inertia forces is increased, i.e. at higher Re^*, Eq. (21) predicts that the variation of the rate of energy absorption $-F_R u_{sh}$ will precede the variation of shaft velocity by an increasing phase difference δ (which however will never exceed the value $\pi/2$). This is confirmed by Figs. 12(b), 19(a) and (b), where higher frequencies are seen to correspond to larger δ. A consequence is that the maximum energy absorption occurs not when the shaft velocity is maximum, like in the low Re^* cases, but earlier. It is a matter of balance between viscous and inertia forces: as the shaft accelerates from a still position (maximum displacement) to its maximum velocity position (zero displacement) the velocity rises but the acceleration drops. Accordingly, viscous forces rise from zero to their maximum, while inertial forces drop from their maximum to zero; the maximum rate of energy absorption occurs somewhere in between. This situation is similar to that described by Iwatsu et al. [19] for the oscillating lid driven cavity problem, who report that the time lag between the lid force and the lid velocity increases with frequency.

Another consequence of the phase difference δ, which can be seen clearly only in Fig. 19(b), is that, roughly during the shaft acceleration phase, the rate of energy absorption (blue curve) is larger than the rate of viscous dissipation (red curve) because some of the absorbed energy becomes kinetic energy of the fluid rather than being dissipated. Conversely, during the shaft deceleration phase, the rate of viscous dissipation is larger than the rate of energy absorption by the damper, as it is not only this absorbed energy but also the kinetic energy of the contained fluid that are dissipated. But the integrals of both lines in Fig. 19(b) over an integer number of cycles must be equal (if slip is neglected), because the kinetic energy at $t = t_0$ is equal to that at $t = t_0 + kT$ for k integer and therefore all the absorbed energy has been converted to heat.

The fact that $\delta > 0$ also means that $\cos\delta + \cos(2\omega t+\delta)$ will necessarily become negative during certain time intervals, because $\cos\delta < 1$. Indeed, this can be seen in Fig. 19(b), where $-F_R u_{sh}$ becomes negative during short time intervals just before the shaft becomes still. During these time intervals the flow of energy is reversed, i.e. instead of going from the shaft to the fluid it returns from the fluid (kinetic energy) to the shaft (mechanical energy). The fact that $-F_R u_{sh} < 0$ means that F_R and u_{sh} have the same sign, so that during such a time interval as the shaft is decelerating, instead of having to push away the fluid in front of it, it is pushed forward by the fluid behind it. This is because the fluid has acquired momentum in the direction of the shaft motion, and the inertia of the fluid is significant.

The maximum rate of work is roughly proportional to the constant c' in (21), which increases with ω, so that increasing the frequency results in higher rates of energy absorption. This can be seen in Figs. 12(b), 19(a) and (b), but the exact relationship between the magnitude of energy absorption and ω is a bit complicated and things are made even more complicated by the fact that in the figures the rate of work is normalised by $\phi_{\text{ref}}\Omega_{\text{tot}}$ (see caption of Fig. 12) which also depends on ω, through the velocity U (Eq. (17)).

This simplified analysis is useful, but it has its limitations. In Fig. 19(b) it may be seen that for $f = 8$ Hz the integral of the dissipation function is not exactly proportional to the shaft velocity. In particular, its value is minimum but non-zero when the shaft velocity is zero. In fact the dissipation function is never zero because the fluid never ceases to flow, due to inertia, even when the shaft is still. This is demonstrated in Fig. 11(f), which shows a plot of the dissipation function for $f = 8$ Hz at a time instance when the shaft is still. On the other hand, maximum energy dissipation occurs when the shaft velocity is maximum, as in Fig. 11(e), where one can notice the asymmetry that is due to the substantial inertia of the fluid. One can also notice in the same Figure the increased importance of the regions near the shaft endpoints in terms of energy dissipation, where the increased velocities at high frequencies produce high velocity gradients, and reduce the role of viscoplasticity.

5. Conclusions

In this paper we studied numerically the viscoplastic flow in an extrusion damper where a sinusoidal displacement is forced on the damper shaft. The flow is assumed axisymmetric, and, except when the shaft is bulgeless, the shape of the domain changes with time. To cope with this, a finite volume method applicable to moving grids was employed. As the calculation of the force on the shaft is crucial, the usual no-slip boundary condition is inappropriate due to the velocity discontinuities at the shaft endpoints, and the Navier slip boundary condition was employed instead. A series of

simulations was performed, where several parameters were varied, in order to study the effects of viscoplasticity, slip, damper geometry, and oscillation frequency on the damper response.

The reciprocating motion of the bulged shaft creates a ring-shaped flow around the bulge, as the latter pushes away the fluid in front of it; away from the bulge the fluid motion is very weak. The bulge creates a stenosis through which the fluid is pushed ("extruded"). In order to overcome the resisting viscous stresses and push the fluid across, high pressure gradients develop; in turn these result in pressure differences between the two sides of the bulge that give rise to significant pressure forces. These pressure forces are the major contribution of the bulge to the total reaction force, and they are larger when the constriction is narrower, i.e. when the bulge diameter is larger or when the outer cylinder diameter is smaller.

The bulgeless case, an annular analogue of the lid-driven cavity problem, was studied as well. It was shown that at low Reynolds numbers, away from the damper end walls, the flow can be approximated very accurately by annular Couette–Poiseuille flow where the pressure gradient is precisely that required for zero net flow across the annulus. The flow pattern is different from the bulged case, with most of the flow occurring in a thin layer surrounding the shaft; the radius of the outer cylinder plays a minor role in this case.

The more viscoplastic the flow is the less the force varies during the damper operation. This is often desirable, because it maximises the energy absorbed for a given force capacity. In combination with slip, viscoplasticity can result in a situation where the shaft moves while the fluid is unyielded and stationary. In this case, but also in every case that there is slip, even if the fluid is yielded, mechanical energy is dissipated not only in the bulk of the fluid due to deformation, but also directly at the fluid-shaft interface due to friction. The percentage of energy lost in this way can be significant if the slip coefficient is large, but also if the yield stress is high (these two are combined in the dimensionless slip coefficient $\tilde{\beta}$).

Increasing the frequency of oscillation makes the inertia of the system more significant and introduces hysteresis into the damper response to the sinusoidal forcing. It also brings the kinetic energy of the fluid into the energy balance, introducing a phase shift of the energy absorption rate relative to the sinusoidal forcing. Furthermore, increasing the frequency weakens the viscoplastic character of the damper response, i.e. it results in greater dependency of the reaction force on the shaft velocity.

Plots of the dissipation function reveal that most of the energy dissipation occurs near the outer part of the bulge and near the shaft ends. When the constriction between the bulge and the outer cylinder is narrow, high dissipation occurs also at the outer cylinder, at the region opposite to the bulge. At the shaft ends there develop high velocity gradients, even when slip occurs. However, these high velocity gradients contribute less to the overall force when the flow is more viscoplastic.

Overall, a two-dimensional simulation can reveal more details about the operation of a damper than a simplified one-dimensional analysis. The present work investigated only dampers operating with Bingham fluids, but in practice the fluids used may exhibit more rheologically complex behaviour, possibly with temperature effects, shear-thinning, viscoelasticity, and thixotropy. The present methodology could be extended to cover these cases as well.

Acknowledgments

This research was funded by the Thales Project "COVISCO" (grant number 648) and the bilateral Greece - Israel Project named PHARMAMUDS (grant number 3163), which are co-funded by Greece and the European Union.

Appendix A. Annular Couette and Couette–Poiseuille flow of a Bingham fluid

Consider first the steady, annular Couette flow of a Bingham fluid between two concentric cylinders of infinite length, of which the inner one, of radius R_i, moves with a constant velocity U in the axial direction while the outer one, of radius R_o, is stationary. The pressure gradient is zero, the only non-zero velocity component is the axial component u, and the only non-zero stress component is τ_{rx}. The flow is one-dimensional and steady so that $u = u(r)$ and $\tau_{rx} = \tau_{rx}(r)$ are functions only of the radial coordinate r. No-slip boundary conditions are assumed. This flow has an analytical solution which is presented in [3], but the location of the yield line is not given there explicitly in closed form. Here we will do so with the help of the Lambert W function [67]. For this flow, the momentum equation simplifies to

$$\tau_{rx} = \frac{c}{r} \tag{A.1}$$

for some constant c. Therefore, the stress decreases monotonically from $r = R_i$ to $r = R_o$ and thus it is maximum at R_i. Since the relative motion between the cylinders implies that yielding is always present, the inner cylinder is always in contact with yielded material and the stress there exceeds the yield stress. Substituting the one-dimensional version of the constitutive equation (4) into Eq. (A.1), integrating, and using the boundary condition that $u(R_i) = U$, we arrive at the following equation which is valid from $r = R_i$ up to any radius where the material is yielded:

$$\frac{u}{U} = 1 - \frac{c}{\mu U}\ln\left(\frac{r}{R_i}\right) + \frac{\tau_y}{\mu U}(r - R_i) \tag{A.2}$$

Let us assume at first that the yielded region extends up to the outer cylinder, i.e. that R_o is not large enough for τ_{rx} to fall below τ_y. Using the boundary condition $u(R_o) = 0$ we can determine the constant c:

$$c = \frac{\tau_y(R_o - R_i) + \mu U}{\ln(R_o/R_i)} \tag{A.3}$$

This can then be substituted in Eq. (A.2) to obtain the velocity:

$$\frac{u}{U} = 1 - \frac{\ln(\tilde{r})}{\ln(\tilde{R}_o)} - Bn\left[\frac{\ln(\tilde{r})}{\ln(\tilde{R}_o)} - \frac{\tilde{r} - 1}{\tilde{R}_o - 1}\right] \tag{A.4}$$

where $\tilde{r} \equiv r/R_i$, $\tilde{R}_o \equiv R_o/R_i$ and Bn is the familiar Bingham number, Eq. (7) (with $H = R_o - R_i$, as usual). The term in square brackets in (A.4) is always positive, or zero for $r = R_i$ ($\tilde{r} = 1$) and $r = R_o$ ($\tilde{r} = \tilde{R}_o$), so that increasing the Bingham number reduces the velocity. Eq. (A.4) is valid as long as the stress at R_o has not fallen below τ_y. The larger R_o the lower $\tau_{rx}(R_o)$ will be; for all the material to be yielded R_o must not exceed a value, say R_y, such that $\tau_{rx}(R_y) = \tau_y$, or, using Eqs. (A.1) and (A.3):

$$\frac{\tau_y(R_y - R_i) + \mu U}{\ln(R_y/R_i)} \cdot \frac{1}{R_y} = \tau_y$$

Employing the alternative Bingham number

$$B \equiv \tau_y R_i/(\mu U) \tag{A.5}$$

which is based on the radius R_i instead of the gap $H = R_o - R_i$, as well as the ratio

$$\tilde{R}_y \equiv R_y/R_i \tag{A.6}$$

after some rearrangement, one obtains:

$$\tilde{R}_y\left(\ln\tilde{R}_y - 1\right) = B^{-1} - 1$$

This equation can be solved using the Lambert W function, which is the inverse function of $f(x) = xe^x$: $xe^x = y \Leftrightarrow x = W(y)$. Noting that $1 = \ln e$, we can manipulate the above equation to get:

$$\tilde{R}_y = e^{W\left(\frac{B^{-1}-1}{e}\right)+1} \tag{A.7}$$

The Lambert W function is double-valued on the interval $(-1/e, 0)$, where we follow its upper branch because the lower branch results in $\tilde{R}_y < 1$, an unrealistic result.

So, for $R_i < R_o \leq R_y$ the velocity is given by Eq. (A.4). What happens when $R_o > R_y$? In that case, at the outer cylinder $\tau_{rx} < \tau_y$ and therefore that cylinder is in contact with a layer of unyielded material, where the velocity is zero due to the no-slip boundary condition and the fact that the outer cylinder is stationary. So, in this case there are two layers of fluid: a yielded one in contact with the inner cylinder, and an unyielded one in contact with the outer cylinder. The velocity variation in the yielded layer together with the location of the interface between the two layers can be found from Eq. (A.2) by using the boundary conditions $u = 0$ and $\tau_{rx} = \tau_y$ at the interface. But we have already done that; the location of the interface is R_y, Eq. (A.7), and the velocity is given by Eq. (A.4) with R_o replaced by R_y. With a little manipulation the result for this partially yielded case is

$$\begin{cases} \dfrac{u}{U} = 1 - \dfrac{\ln(\tilde{r})}{\ln(\tilde{R}_y)} \\ \quad -B(\tilde{R}_y - 1)\left[\dfrac{\ln(\tilde{r})}{\ln(\tilde{R}_y)} - \dfrac{\tilde{r}-1}{\tilde{R}_y - 1}\right], & R_i \leq r \leq R_y \\ u = 0, & R_y \leq r \leq R_o \end{cases} \tag{A.8}$$

The thickness of the yielded layer $\tilde{R}_y - 1$ is a strictly decreasing function of B. We note that according to Eqs. (A.7) and (A.8) the thickness and the velocity of the yielded layer are independent of the outer cylinder diameter, contrary to the fully yielded case (Eq. (A.4)). This is reflected in the use of B instead of Bn in the partially yielded case.

Next, consider the case of annular Couette–Poiseuille flow, i.e. let there also be an axial pressure gradient $\mathrm{d}p/\mathrm{d}x \neq 0$. This case can be solved in a similar manner, but it is more complex and there are many possible flow types depending on the importance of the pressure gradient relative to the inner cylinder velocity. All the possibilities are reported by Liu and Zhu [29], but here we are only interested in the case where the pressure gradient opposes the cylinder motion and causes a zero net flow through any annular section. This may be a good approximation to the flow in an annular cavity, where the sides of the cavity restrict the flow in the axial direction. This case falls under "Case I" of Liu and Zhu [29], and the flow pattern consists of two yielded layers adjacent to the two cylinders, with an unyielded layer in between. The inner yielded layer moves mostly along with the inner cylinder, but its outer part moves in the opposite direction; the unyielded layer and the outer yielded layer move opposite to the inner cylinder. Suppose the yield lines are at $r = y_1$ and y_2 ($\tilde{r} = \tilde{y}_1$ and $\tilde{y}_2$). Then the velocity is given by

$$\begin{cases} \dfrac{u}{U} = 1 + B(\tilde{r} - 1) + \frac{1}{4}P(\tilde{r}^2 - 1) \\ \quad - \left(B\tilde{y}_1 + \frac{1}{2}P\tilde{y}_1^2\right)\ln(\tilde{r}), & R_i \leq r \leq y_1 \\ u = u(y_1) = u(y_2), & y_1 < r < y_2 \\ \dfrac{u}{U} = B(\tilde{R}_o - \tilde{r}) - \frac{1}{4}P(\tilde{R}_o^2 - \tilde{r}^2) \\ \quad + \left(B\tilde{y}_2 - \frac{1}{2}P\tilde{y}_2^2\right)\ln\left(\dfrac{\tilde{r}}{\tilde{R}_o}\right), & y_2 \leq r \leq R_o \end{cases} \tag{A.9}$$

where P is a dimensionless pressure gradient

$$P \equiv \frac{\mathrm{d}p}{\mathrm{d}x}\frac{R_i^2}{\mu U} \tag{A.10}$$

The yield lines can be found from the fact that the velocities are equal there, $u(y_1) = u(y_2)$, using also the relation

$$\tilde{y}_2 = \tilde{y}_1 + 2B/P \tag{A.11}$$

which derives from the momentum balance on the unyielded layer. The result is

$$1 + B\left(\frac{B}{P} - \tilde{R}_o - 1\right) + \frac{1}{4}P(\tilde{R}_o^2 - 1) + B\tilde{y}_1 + \left(B\tilde{y}_1 + \frac{1}{2}P\tilde{y}_1^2\right)\ln\left(\frac{\tilde{y}_1 + 2B/P}{\tilde{R}_o\tilde{y}_1}\right) = 0 \tag{A.12}$$

Eq. (A.12) can be solved numerically to obtain $\tilde{y}_1$, and then $\tilde{y}_2$ is obtained from (A.11). Thus Eq. (A.9) contains no unknown terms and can be integrated to obtain the flow rate $Q = 2\pi\int_{R_i}^{R_o} u\mathrm{d}r$. For a given geometry, fluid, and inner cylinder velocity, the flow rate depends on the pressure gradient, $Q = Q(P)$. We seek the pressure gradient that results in $Q(P) = 0$. This is solved numerically in the present work, using the Newton–Raphson method, with $\mathrm{d}Q/\mathrm{d}P$ calculated numerically by perturbing Q. The results shown in Fig. 15 were obtained in this manner.

For completeness, we also give the velocity when the flow is Newtonian (also shown in Fig. 15(b)):

$$\frac{u}{U} = 1 + \frac{1}{4}P(\tilde{r}^2 - 1) - \left[1 + \frac{1}{4}P(\tilde{R}_o^2 - 1)\right]\frac{\ln(\tilde{r})}{\ln(\tilde{R}_o)} \tag{A.13}$$

References

[1] M.C. Constantinou, M.D. Symans, Experimental study of seismic response of buildings with supplemental fluid dampers, Struct. Des. Tall Build. 2 (1993) 93–132.
[2] C.-Y. Hou, Fluid dynamics and behavior of nonlinear viscous fluid dampers, J. Struct. Eng. 134 (1) (2008) 56–63.
[3] R.B. Bird, G. Dai, B.J. Yarusso, The rheology and flow of viscoplastic materials, Rev. Chem. Eng. 1 (1) (1982) 1–70.
[4] H.A. Barnes, The yield stress - a review or '$\pi\alpha\nu\tau\alpha\rho\varepsilon\iota$' - everything flows? J. Non-Newton. Fluid Mech. 81 (1999) 133–178.
[5] N.J. Balmforth, I.A. Frigaard, G. Ovarlez, Yielding to stress: recent developments in viscoplastic fluid mechanics, Annu. Rev. Fluid Mech. 46 (2014) 121–146.
[6] S. Genc, P.P. Phulé, Rheological properties of magnetorheological fluids, Smart Mater. Struct. 11 (1) (2002) 140.
[7] D. Susan-Resiga, A rheological model for magneto-rheological fluids, J. Intell. Mater. Syst. Struct. (2009).
[8] W. Robinson, L. Greenbank, An extrusion energy absorber suitable for the protection of structures during an earthquake, Earthq. Eng. Struct. Dyn. 4 (3) (1976) 251–259.
[9] W. Cousins, T. Porritt, Improvements to lead-extrusion damper technology, Bull. N. Z. Natl. Soc. Earthq. Eng. 26 (3) (1993) 342–348.
[10] G.W. Rodgers, J.G. Chase, J.B. Mander, N.C. Leach, C.S. Denmead, Experimental development, tradeoff analysis and design implementation of high force–to-volume damping technology, Bull. N. Z. Natl. Soc. Earthq. Eng. 40 (2) (2007) 35–48.
[11] N. Makris, 2013, Private communication.
[12] N.M. Wereley, L. Pang, Nondimensional analysis of semi-active electrorheological and magnetorheological dampers using approximate parallel plate models, Smart Mater. Struct. 7 (5) (1998) 732.
[13] X. Wang, F. Gordaninejad, Flow analysis and modeling of field-controllable, electro-and magneto-rheological fluid dampers, J. Appl. Mech. 74 (1) (2007) 13–22.
[14] Q.-H. Nguyen, S.-B. Choi, Dynamic modeling of an electrorheological damper considering the unsteady behavior of electrorheological fluid flow, Smart Mater. Struct. 18 (5) (2009) 055016.
[15] M. Yu, S. Wang, J. Fu, Y. Peng, Unsteady analysis for oscillatory flow of magnetorheological fluid dampers based on Bingham plastic and Herschel–Bulkley models, J. Intell. Mater. Syst. Struct. 24 (2013) 1067–1078.
[16] N. Makris, S.A. Burton, D. Hill, M. Jordan, Analysis and design of ER damper for seismic protection of structures, J. Eng. Mech. 122 (10) (1996) 1003–1011.
[17] Z. Parlak, T. Engin, Time-dependent CFD and quasi-static analysis of magnetorheological fluid dampers with experimental validation, Int. J. Mech. Sci. 64 (1) (2012) 22–31.
[18] H. Blackburn, J. Lopez, Modulated waves in a periodically driven annular cavity, J. Fluid Mech. 667 (2011) 336–357.
[19] R. Iwatsu, J.M. Hyun, K. Kuwahara, Numerical simulation of flows driven by a torsionally oscillating lid in a square cavity, J. Fluids Eng. 114 (2) (1992) 143–151.
[20] S.S. Mendu, P. Das, Fluid flow in a cavity driven by an oscillating lid - a simulation by lattice Boltzmann method, Eur. J. Mech.-B/Fluids 39 (2013) 59–70.
[21] N.J. Balmforth, Y. Forterre, O. Pouliquen, The viscoplastic Stokes layer, J. Non-Newton. Fluid Mech. 158 (1) (2009) 46–53.
[22] C.R. McArdle, D. Pritchard, S.K. Wilson, The Stokes boundary layer for a thixotropic or antithixotropic fluid, J. Non-Newton. Fluid Mech. 185 (2012) 18–38.

[23] A.-R. Khaled, K. Vafai, The effect of the slip condition on Stokes and Couette flows due to an oscillating wall: exact solutions, Int. J. Non-Linear Mech. 39 (5) (2004) 795–809.
[24] W.M. Laird, Slurry and suspension transport – basic flow studies on Bingham plastic fluids, Ind. Eng. Chem. 49 (1) (1957) 138–141.
[25] A. Fredrickson, R.B. Bird, Non-Newtonian flow in annuli, Ind. Eng. Chem. 50 (3) (1958) 347–352.
[26] E.J. Fordham, S.H. Bittleston, M.A. Tehrani, Viscoplastic flow in centered annuli, pipes, and slots, Ind. Eng. Chem. Res. 30 (3) (1991) 517–524.
[27] P.O. Brunn, B. Abu-Jdayil, Axial annular flow of plastic fluids: dead zones and plug-free flow, Rheol. acta 46 (4) (2007) 449–454.
[28] D.M. Kalyon, M. Malik, Axial laminar flow of viscoplastic fluids in a concentric annulus subject to wall slip, Rheol. Acta 51 (9) (2012) 805–820.
[29] Y.-Q. Liu, K.-Q. Zhu, Axial Couette–Poiseuille flow of Bingham fluids through concentric annuli, J. Non-Newton. Fluid Mech. 165 (21) (2010) 1494–1504.
[30] P. Filip, J. David, Axial Couette–Poiseuille flow of power-law viscoplastic fluids in concentric annuli, J. Petrol. Sci. Eng. 40 (3) (2003) 111–119.
[31] I. Daprà, G. Scarpi, Pulsatile Poiseuille flow of a viscoplastic fluid in the gap between coaxial cylinders, J. Fluids Eng. 133 (8) (2011) 081203.
[32] G.K. Batchelor, An introduction to fluid dynamics, Cambridge University Press, 2000. Pages 224–227.
[33] J. Koplik, J.R. Banavar, Corner flow in the sliding plate problem, Phys. Fluids 7 (12) (1995) 3118–3125.
[34] T. Qian, X.-P. Wang, Driven cavity flow: from molecular dynamics to continuum hydrodynamics, Multiscale Model. Simulat. 3 (4) (2005) 749–763.
[35] T. Sochi, Slip at fluid-solid interface, Polym. Rev. 51 (4) (2011) 309–340.
[36] Q. He, X.-P. Wang, Numerical study of the effect of Navier slip on the driven cavity flow, ZAMM-J. Appl. Math. Mech. 89 (10) (2009) 857–868.
[37] D.M. Kalyon, Apparent slip and viscoplasticity of concentrated suspensions, J. Rheol. 49 (3) (2005) 621–640.
[38] S.G. Hatzikiriakos, Wall slip of molten polymers, Progr. Polym. Sci. 37 (4) (2012) 624–643.
[39] Y. Damianou, M. Philippou, G. Kaoullas, G.C. Georgiou, Cessation of viscoplastic Poiseuille flow with wall slip, J. Non-Newton. Fluid Mech. 203 (2014) 24–37.
[40] N. Nirmalkar, R. Chhabra, R. Poole, Laminar forced convection heat transfer from a heated square cylinder in a Bingham plastic fluid, Int. J. Heat Mass Transf. 56 (2013) 625–639.
[41] M.D. Symans, M.C. Constantinou, Semi-active control systems for seismic protection of structures: a state-of-the-art review, Eng. Struct. 21 (1999) 469–487.
[42] H. Bašić, I. Demirdžić, S. Muzaferija, Finite volume method for simulation of extrusion processes, Int. J. Numer. Methods Eng. 62 (2005) 475–494.
[43] A. Williams, A. Slone, T. Croft, M. Cross, A mixed Eulerian–Lagrangian method for modelling metal extrusion processes, Comput. Methods Appl. Mech. Eng. 199 (2010) 2123–2134.
[44] A. Syrakos, A. Goulas, Estimate of the truncation error of finite volume discretization of the Navier–Stokes equations on colocated grids, Int. J. Numer. Methods Fluids 50 (1) (2006) 103–130, doi:10.1002/fld.1038.
[45] A. Syrakos, G. Georgiou, A. Alexandrou, Solution of the square lid-driven cavity flow of a Bingham plastic using the finite volume method, J. Non-Newton. Fluid Mech. 195 (2013) 19–31.
[46] C. Rhie, W. Chow, Numerical study of the turbulent flow past an airfoil with trailing edge separation, AIAA J. 21 (11) (1983) 1525–1532.
[47] S. Muzaferija, D. Gosman, Finite-volume CFD procedure and adaptive error control strategy for grids of arbitrary topology, J. Comput. Phys. 138 (2) (1997) 766–787.
[48] J.H. Ferziger, M. Peric, Computational Methods for Fluid Dynamics, 3rd edition, Springer, 2002.
[49] I. Demirdžić, M. Perić, Space conservation law in finite volume calculations of fluid flow, Int. J. Numer. Methods Fluids 8 (1988) 1037–1050.
[50] I.A. Frigaard, C. Nouar, On the usage of viscosity regularisation methods for visco-plastic fluid flow computation, J. Non-Newton. Fluid Mech. 127 (2005) 1–26.
[51] T.C. Papanastasiou, Flows of materials with yield, J. Rheol. 31 (1987) 385–404.
[52] G. Karapetsas, J. Tsamopoulos, Transient squeeze flow of viscoplastic materials, J. Non-Newton. Fluid Mech. 133 (2006) 35–56.
[53] Y. Dimakopoulos, J. Tsamopoulos, Transient displacement of Newtonian and viscoplastic liquids by air in complex tubes, J. Non-Newton. Fluid Mech. 142 (2007) 162–182.
[54] J. Tsamopoulos, Y. Dimakopoulos, N. Chatzidai, G. Karapetsas, M. Pavlidis, Steady bubble rise and deformation in Newtonian and viscoplastic fluids and conditions for bubble entrapment, J. Fluid Mech. 601 (2008) 123–164.
[55] J. Papaioannou, G. Karapetsas, Y. Dimakopoulos, J. Tsamopoulos, Injection of a viscoplastic material inside a tube or between two parallel disks: conditions for wall detachment of the advancing front, J. Rheol. 53 (5) (2009) 1155–1191.
[56] G.R. Burgos, A.N. Alexandrou, V. Entov, On the determination of yield surfaces in Herschel–Bulkley fluids, J. Rheol. 43 (1999) 463–483.
[57] A. Syrakos, G.C. Georgiou, A.N. Alexandrou, Performance of the finite volume method in solving regularised Bingham flows: inertia effects in the lid-driven cavity flow, J. Non-Newton. Fluid Mech. 208–209 (2014) 88–107.
[58] Y. Dimakopoulos, M. Pavlidis, J. Tsamopoulos, Steady bubble rise in Herschel–Bulkley fluids and comparison of predictions via the Augmented Lagrangian Method with those via the Papanastasiou model, J. Non-Newton. Fluid Mech. 200 (2013) 34–51.
[59] R. Glowinski, A. Wachs, On the numerical simulation of viscoplastic fluid flow, in: R. Glowinski, J. Xu (Eds.), Numerical Methods for Non-Newtonian Fluids, Handbook of Numerical Analysis, 16, Elsevier, 2011, pp. 483–717.
[60] S.V. Patankar, D.B. Spalding, A calculation procedure for heat, mass and momentum transfer in three-dimensional parabolic flows, Int. J. Heat Mass Transf. 15 (1972) 1787–1806.
[61] P. Khosla, S. Rubin, A diagonally dominant second-order accurate implicit scheme, Comput. Fluids 2 (1974) 207–209.
[62] L. Ferrás, J. Nóbrega, F. Pinho, Implementation of slip boundary conditions in the finite volume method: new techniques, Int. J. Numer. Methods Fluids 72 (7) (2013) 724–747.
[63] H.H. Winter, Viscous dissipation term in energy equations, in: Modular Instruction Series C: Calculation and Measurement Techniques for Momentum, Energy and Mass Transfer, Vol. 7, American Institute of Chemical Engineers: New York, 1987, pp. 27–34.
[64] Y. Damianou, G.C. Georgiou, Viscoplastic poiseuille flow in a rectangular duct with wall slip, J. Non-Newton. Fluid Mech. 214 (2014) 88–105.
[65] A.N. Beris, J.A. Tsamopoulos, R.C. Armstrong, R.A. Brown, Creeping motion of a sphere through a Bingham plastic, J. Fluid Mech. 158 (1985) 219–244.
[66] W. Li, G. Yao, G. Chen, S. Yeo, F. Yap, Testing and steady state modeling of a linear MR damper under sinusoidal loading, Smart Mater. Struct. 9 (1) (2000) 95.
[67] R.M. Corless, G.H. Gonnet, D.E. Hare, D.J. Jeffrey, D.E. Knuth, On the Lambert W function, Adv. Comput. Math. 5 (1996) 329–359.